Phase separation, transformation and domain formation in $LaNbO_4$ supersaturated with Sr

A TEM study

Øystein Prytz

Thesis submitted in partial fulfillment
of the requirements for the degree of
Candidatus scientiarum

Department of Physics
University of Oslo

May 2003

Phase separation, transformation and domain formation in $LaNbO_4$ supersaturated with Sr

A TEM study

Øystein Prytz

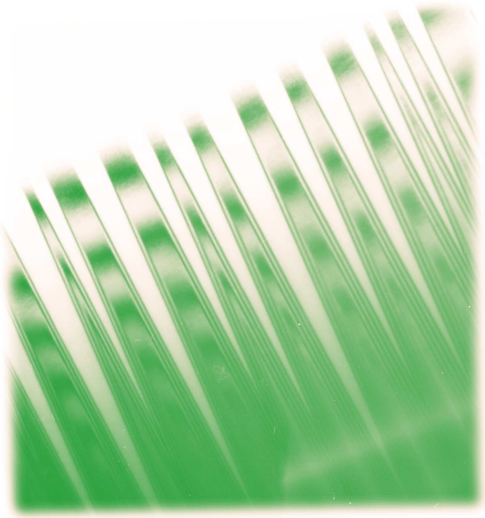

Thesis submitted in partial fulfillment
of the requirements for the degree of
Candidatus scientiarum

Department of Physics
University of Oslo

May 2003

Preface

Work on this thesis was mainly carried out during the autumn of 2002 and spring of 2003 at the Centre for Materials Science at the University of Oslo. Many people have contributed quite a lot to the successful completion of this thesis, and I would like to use this opportunity to thank them all.

First and foremost I would like to thank my supervisors Johan Taftø and Truls Norby, both for suggesting an interesting project and for their guidance along the way. An additional thanks is due to Johan Taftø for the hours and hours of fun and interesting discussions, both on and off topic. I would also like to thank Arne Olsen for useful discussions, Erik Sørbrøden for skillful assistance with TEM, Anette Gunnæs for help with specimen preparation and dr. Yurii M. Baikov for providing the samples used.

Furthermore, I would like to give a big thanks to the students and employees at The Department of Physics for making my stay at the University a pleasant one. I can not imagine how I would have completed this project without their encouragement. I would also like to thank Martin Foss for stirring my interest for materials science.

Finally, many thanks to my family for their encouragement and support throughout my education.

Øystein Prytz
May 2003

Summary

We have studied the lanthanum niobate system doped with strontium of nominal composition $La_{0.95}Sr_{0.05}NbO_4$. We observe two phases in the synthesized material. One of these phases is Sr-poor $LaNbO_4$. The other phase is to our knowledge an unreported oxide with a Sr:Nb ratio between 1:3 and 1:2. This phase has a large unit cell with lattice parameters $a = 7.91$Å, $b = 5.81$Å and $c = 30.75$Å.

The well known Sr-poor phase, $LaNbO_4$, transforms from a tetragonal to a monoclinic crystal structure upon cooling. This transformation is accompanied by domain formation. The observed orientation of the domain boundaries is in excellent agreement with theoretical considerations presented in this thesis. Furthermore, we have studied the atomic arrangement at the domain boundary by high resolution electron microscopy, and observe that the boundary is highly ordered.

Contents

List of Figures

List of Tables

Chapter 1

Introduction

The world energy consumption has exploded the past 150 years. The increase has mainly occured in the industrialized part of the world, and is a fundamental basis for modern lifestyle. As the 3rd World steadily increases the standard of living for its population, the total consumption is expected to rise. Combined with increased consumption in the industrialized world, it is expected that this will cause a growth in total world energy consumption of 60% compared to 1999 by 2020 [1], see table 1.1.

Table 1.1: Projections of world energy consumption (10^{15} Btu). Source: International Energy Outlook 2002 [1]

Region	1999	2010	2020
Industrial World	209.7	246.6	277.8
E. Europe/Russia	50.4	61.8	73.4
Developing Countries	121.8	184.1	260.3
Total	381.9	492.6	611.5

Fossil fuels are currently the most used source, supplying some 80% of the total world energy consumption. Projections done by the US Department of Energy, show fossil fuels supplying stable, or increasing, shares of the growing world energy consumption [1]. Although our reserves of coal, oil and natural gas are still abundant, the increasing rate of depletion will eventually cause rising prices some time during the next few decades.

In the last 10-15 years there has been growing consensus in the scientific community about the environmental problems caused by the burning of fossil fuels. Mounting evidence suggests that emission of large amounts of CO_2 are causing a stronger 'greenhouse' effect and heating of the atmosphere. In addition there are concerns about the environmental damage caused by NO_x and SO_x released in the burning of fossil fuels. Increased use of fossil fuels will most probably cause unacceptable enviromental damage, and steps are being taken to reduce the global emission of greenhouse gasses (e.g. the Kyoto-agreement).

In light of the expected increase in energy consumption, the rising cost of fossil fuels and the growing environmental concerns, there is increased interest for future sources of energy and the technology for their use. The criteria, however, for successful implementation of new energy technologies are not easily met. To be deemed both politically and economically acceptable, the new technologies must be capable of supporting dramatic increases of living standards in the less developed world, moderate increases in living standards in the western world, and both of these with less damage to the environment and at lower costs

than today's petroleum based technology. The challenge this presents to scientists and engineers can hardly be overestimated.

Dresselhaus and Thomas [2] have explored some possible alternative sources for energy. In the short term, however, one should not be too optimistic about large scale exploitation of alternative sources of energy. The technology and economy of most of these sources are still far from adequate, and fossil fuels are expected to play a major role in supplying the world with the energy needed for decades to come. It is therefore important to consider if these resources can be exploited more efficiently, and with less harm to the environment.

One likely prospect in this regard is the gradual introduction of fuel cell-based power sources. Conversion of chemical energy by way of fuel cells promises to be far more efficient than conversion by way of combustion, the common process today. The various fuel cell technologies have potentially a very wide span of application, from small handheld devices, possible use for automotive purposes, to large stationary powerplants.

However, the development of more efficient, economical and practical fuel cells depends heavily on our ability to develop more suitable materials for the various components of the cell. The materials used in prototypes today are often expensive and may have been selected two-three decades ago. Internationally there is increased effort to identify promising new materials for the various components of the fuel cells, see Steele and Heinzel [3] for a review.

Students and scientists at the Centre for Materials Science, University of Oslo, are currently studying ceramic materials with fluorite related structures. Many of these materials show promise for use as electro-catalysts and electrolytes in solid-oxide fuel cells.

The main objective of this thesis is to investigate the low temperature phase of *lanthanum orthoniobate*, $LaNbO_4$, doped with Sr. The doping is intended to create charged defects, and thereby increase the material's ion conductivity [4]. There is, however, some uncertainty as to the solubility of Sr in the $LaNbO_4$ matrix. We will investigate whether the doping has been successful, or if the samples have separated into different phases. In the latter case, we will attempt to study the phases involved.

The low temperature phase of $LaNbO_4$ has been reported to have space group symmetry $C2/c$ or $I2/c$ using a non standard setting [5]. The low temperature phase is heavily twinned [6], and there have been some investigations into the orientation and nature of the twin boundaries [6] [7]. We will investigate how the crystal structure and boundary orientations are affected by the Sr doping, and we will furthermore investigate segregation of Sr to the boundaries between twin domains.

Chapter 2

Background and theory

2.1 Structural phase transitions and the occurrence of twinning

Crystals often transform from one crystal structure to another as we vary the temperature or pressure. As with all other phase transitions, these changes occur in an attempt to minimize the free energy of the system. Generally, the high-temperature phase will have a higher symmetry than the low-temperature phase.

We can divide the structural phase transitions into two types. On the one hand there are the transitions where a new lattice is constructed, for example the transition from bcc to fcc iron or the transformation of graphite to diamond. On the other hand there are the transitions where a prototype lattice is somewhat distorted, for example in the transition of a low temperature polymorph of SiO_2 (e.g. quartz) to the associated high-temperature polymorph . We call these reconstructive and distortive transitions respectively. We shall consider the latter.

The distortive transition are the result of slight displacements of atoms in the unit cell, typically causing small changes in the length of the cell axes and the angles between them. For a single crystal without a restraining environment, we would expect the microscopic changes in parameters to cause a corresponding macroscopic deformation. However, in most cases, the sample is not free to deform without regard to the surroundings.

A sample will normally consist of numerous crystal *grains*. These are regions with identical crystal structure, but of different crystallographic orientation. The grain orientations are generally not related through any operation of symmetry, but rather in a random manner.

As the sample is cooled below the transition temperature, each crystal grain will try to expand and contract in a manner consistent with the changes in the unit cell. Since the grains are randomly oriented with regard to each other, two adjacent grains may find themselves trying to expand in opposite directions. This kind of incompatible deformation of the grains will result in a considerable increase of strain-energy in the crystal.

Let us consider the two-dimensional case of a transformation from a square lattice to a rectangular one, see figure 2.1. Although this is a simplification compared to our three-dimensional reality, many systems transform with significant changes only in two dimensions. Our two-dimensional model is therefore useful for understanding many transformations of real systems.

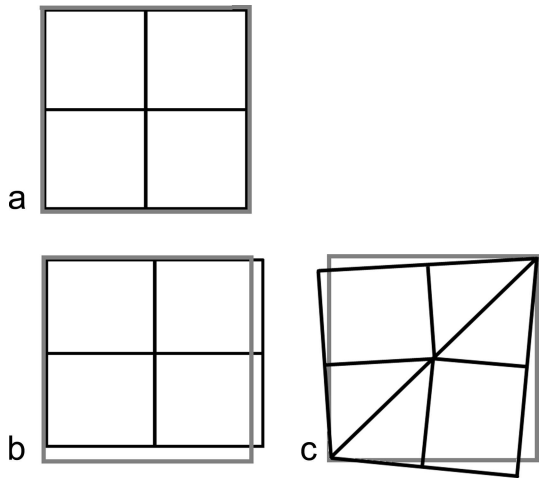

Figure 2.1: **a:** The original square lattice. The size and shape of the grain is marked in grey. **b:** Simply transforming all the unit cells would change the shape of the grain dramatically compared to the original, causing strain incompatability between neighbouring grains. **c:** By introducing a twinning-plane along the diagonal, adjacent grains may be accommodated more easily thereby reducing the strain energy.

The transformation causes a deformation of the grain, increasing its length in one direction, while reducing it in another, figure 2.1(b). The deformation of adjacent grains will generally not accommodate this change, thereby causing a considerable increase in lattice strain-energy when two grains experience conflicting deformations.

To avoid this increase in strain-energy, the grain has to find a way to retain its original macroscopic shape, or at least stay as close to it as possible. This can be achieved by the formation of twin domains in the grain, figure 2.1(c). In this case, the domains are mirror images of each other, with the mirror plane, or *domain boundary*, being the diagonal of the original cell.

The macroscopic effect on the grain of many such twinning domains is shown in figure 2.2. We see that the shape of the transformed grain containing twinned domains is closer to the original shape than the situation without twinning. The strain energy is therefore lowered compared to the untwinned case.

Introduction of twinned domains (or rather their boundaries) is itself associated with a higher configurational energy than that of the perfect lattice. The reason twinning still occurs is that there is a trade-off between the configurational energy and the strain energy: increase one to reduce the other. As long as the net result is a lower total energy, this phenomena can occur.

Crystals that undergo displacive transitions are called *ferroelastic*, and are a subgroup of the ferroic crystals. These are considered in the next section.

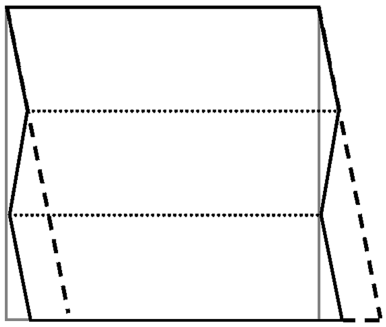

Figure 2.2: The effect of introducing multiple twinned domains in a transformed grain. The grey square indicates the original size of the grain, while the dashed lines outline the grain after transformation if no twinning occured. The grain after twinning is represented by the zig-zagging lines and the domain boundaries are marked by the dotted lines.

2.2 Ferroic crystals

A well known class of materials to all undergraduate students of physics are the *ferromagnetic* materials. These are crystals which, even in the absence of an external magnetic field, possess a magnetization vector. We call this the *spontaneous* magnetization vector. By applying an external magnetic field we may change the direction of this vector. We say that the crystal changes from one orientation state (OS) to another.

Similarly, another well known class of materials are the *ferroelectric* crystals. These are crystals that possess a spontaneous electric polarization vector. The direction of the polarization vector may be changed by the application of an external electric field, thereby causing a transition from one orientation state to another.

These two classes of materials are part of a more general class referred to as the *ferroic* materials. A third group of crystals is also part of this general class, they are referred to as the *ferroelastic* crystals. In complete analogy to the ferromagnetic and ferroelectric systems, these are crystals which, in the absence of external mechanical stress, possess a spontaneous strain tensor. By applying a mechanical stress, the crystal can change from one orientation state to another, thereby changing the spontaneous strain tensor.

Aizu has described the 773 different species of ferroic crystal [8], and determined the orientation states and spontaneous strain tensors for the 94 species of ferroelastic crystals [9].

The origin of the ferroelastic orientation states is a distortive phase transition from one crystal structure to another. Due to the symmetry of the structure before transformation, there may be many equivalent ways for such a transition to occur. As an example, we may conisder the transformation from a cubic to a tetragonal system: here, any one of the three unit cell axes may elongate or contract to produce the tetragonal structure, see figure 2.3.

These three ways of transforming produce the same result: the orientation states are crystallographically and energetically equivalent. This makes it impossible to distinguish one from the other if they appear seperately. In most cases, however, a crystal is likely to exhibit more than one orientation state, and it will then be possible to distinguish them. This applies to all ferroic systems.

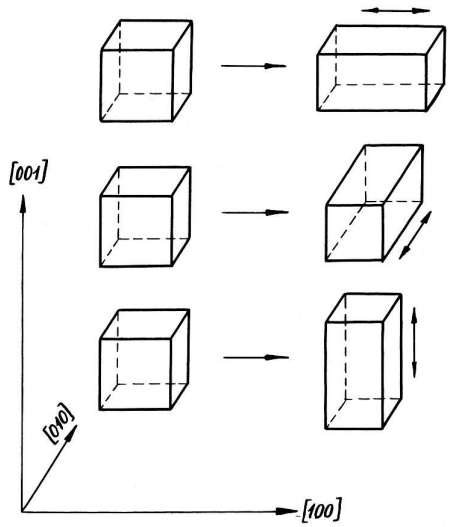

Figure 2.3: An illustration of the three way in which the transformation from a cubic to a tetragonal system may occur. Adapted from Khachaturyan [10].

A region of a sample consisting of a specific orientation state is called a domain, and the boundary between two domains is called the domain wall or domain boundary. Not all domain wall orientations are favourable, the walls will, whenever possible, be oriented so as to maintain strain compatibility between the two neighbouring domains. Sapriel [11] has formulated the domain-wall equations for the ferroelastic species.

We give a short summary of some important properities of the ferroelastic crystals, see Aizu [8] [9] and Sapriel [11]. One may note that many of these properties apply also for other ferroic systems.

1. The ferroelastic crystals are the result of a transition from a high-symmetry *prototypic* phase to a low(er)-symmetry *ferroic* phase. This transition induces the formation of at least two *orientation states*.
2. The orientation states are identical or enantimorphous in structure, and therefore energetically equivalent. They are, however, different in spontaneous strain tensor.
3. We denote the strain tensor of an orientation state S_i as $\mathbf{e}(S_i)$. Schlenker et al. [12] have shown how the components of this strain tensor can be calculated from the lattice parameters of the crystal before and after the transition from the prototypic to the ferroelastic phase.
4. A ferroelastic crystal can change from one orientation state to another by the application of external mechanical stress.
5. If $S_1, S_2, \ldots, S_q$ are the q orientation states of a crystal, the *spontaneous* strain tensor of an orientation state S_i is defined by Aizu [9] as:

$$\mathbf{e}_s(S_i) = \mathbf{e}(S_i) - \frac{1}{q}\sum_{k=1}^{q}\mathbf{e}(S_k) \tag{2.1}$$

6. The prototypic phase is said to belong to the point group L_p, while the ferroelastic phase belongs to the point group L_f with lower symmetry. L_f is a subgroup of L_p, i.e. L_p contains all the symmetry elements of L_f. We denote the elements of L_p which are not contained in L_f as F. That is:

$$L_f \subset L_p \qquad \text{and} \qquad F = (L_f \cap L_p)^c$$

7. All operations of L_f keep the strain tensors, $\mathbf{e}$ and $\mathbf{e}_s$, unchanged, and therefore the orientation state is unchanged under these operations. The operations contained in F, however, cause a change from one orientation state to another. The orientation states are therefore related through the operations of symmetry lost in the transition from the prototypic to the ferroelastic phase. See appendix A.1 for further discussion.

8. The boundary between two domains — the domain wall — is oriented so as to maintain strain compatability between the two domains. More precisely speaking, we assume that the boundaries are planes containing vectors which during the transformation from the prototypic to the ferroelastic phase change an equal amount in both orientation states. Sapriel [11] has expressed this mathematically as:

$$(S_{ij} - S'_{ij})x_i x_j = 0 \tag{2.2}$$

Here S_{ij} and S'_{ij} are the components of the spontaneous strain tensor of the orientation states labeled S and S'. Similarly, x_i and x_j are the components of a vector $\mathbf{x}$ (see appendix A.3). Working from these conditions, Sapriel has determined the equations of all possible domain walls for the 94 species of ferroelastic crystals.

Some of these concepts will be studied more closely in the next section.

2.3 Ferroelastic $LaNbO_4$

$LaNbO_4$ is known to have two polymorphs. At high temperatures it has a tetragonal structure with space group $I4_1/a$ [13] (number 88). This is called the Scheelite-structure, referring to the structure of the mineral Scheelite, $CaWO_4$, named in honour of the Swedish chemist, K. W. Scheele (1742-1786). We present an illustration of the high temperature structure of $LaNbO_4$ in figure 2.4.

The low-temperature phase is monoclinic with space group $C2/c$ [5] (number 15). This structure is often called Fergusonite after the Scottish mineral collector Robert Ferguson (1767–1840).The structure may be regarded as a monoclinic distortion of the tetragonal structure. This relationship may be easier to see if we use the non-conventional setting of an I-centered monoclinic unit cell. The space group is then $I2/c$. The relationship between the I and C lattice is shown in figure 2.5 together with the tetragonal axes in the $[001]$ projection. The tetragonal c_t axis corresponds to the monoclinic b_m axis.

2.3.1 The tetragonal to monoclinic transition

The transition from the tetragonal to the monoclinic phase has been reported to occur in the range of $490°C$ to $525°C$, there is also evidence of the transition being of the second order [14]. This is consistent with viewing the transition as a slight displacement of the atoms, rather than a more dramatic reconstruction of the lattice. The cell parameters of the tetragonal and monoclinic phases are listed in table 2.1.

The significant changes in this transformation take place in the tetragonal $a_t - b_t$ plane; the change in length here is -3% and 3.7%, while the cange in the c_t axis is only about 1.3%. In addition, the angle between

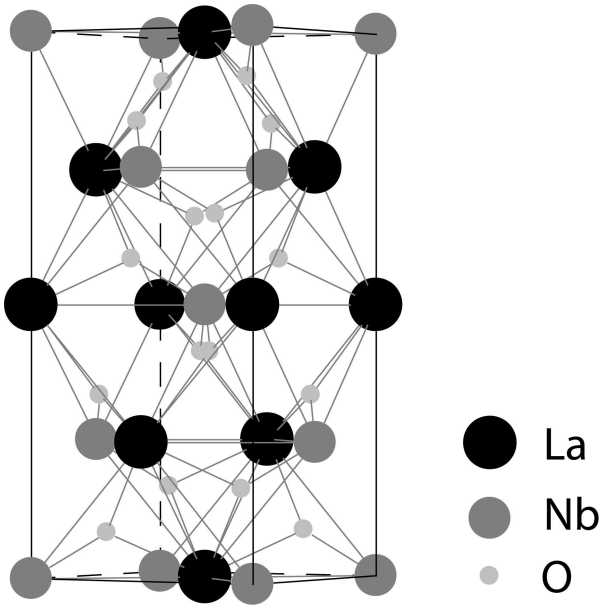

Figure 2.4: The high temperature phase of $LaNbO_4$

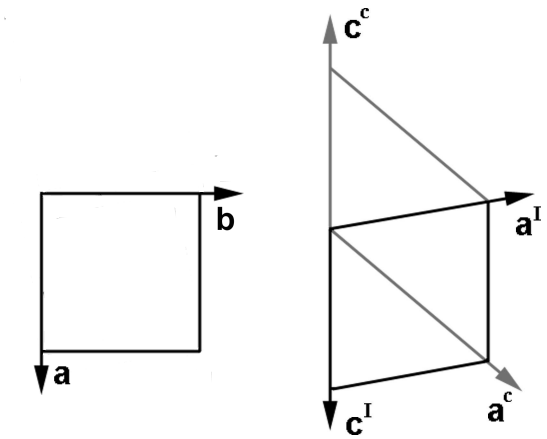

(a) The tetragonal a and b axes seen in the $[001]$ projection.

(b) The relationship between the monoclinic I-lattice (black line) and C-lattice (grey line) seen in the $[010]$ projection.

Figure 2.5: The tetragonal and monoclinic and axes seen in the $[001]_{\mathrm{t}}$ and $[010]_{\mathrm{m}}$ projections respectively

Table 2.1: The cell parameters of the tetragonal and monoclinic phases of $LaNbO_4$. The values for the tetragonal phase are those obtained by David [13] at $530°C$. The values for the monoclinic phase are those obtained by Tsunekawa et al. [15].

	a/Å	b/Å	c/Å	α	β	γ	Space group	Point group
Tetragonal	5.4009	5.4009	11.6741	90°	90°	90°	$I4_1/a$	$4/m$
Monoclinic	5.5647	11.5194	5.2015	90°	94.100°	90°	$I2/c$	$2/m$

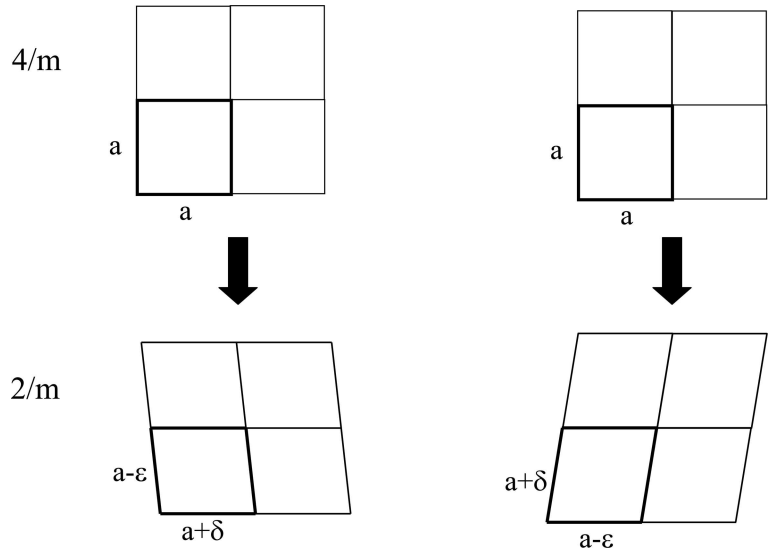

Figure 2.6: The two orientation states for a transformation from tetragonal to monoclinic. Because of the fourfold-symmetry of the prototypic phase there are two possible ways for the unit cell to deform. This results in two orientation states which are identical in structure, but different in orientation.

these two 'short' axes is changed considerably, while the remaining angles are unchanged. We therefore consider the transformation from the two-dimensional viewpoint of the $[001]_{\mathrm{t}}$ or $[010]_{\mathrm{m}}$ projection, see figure 2.5.

During the transformation, one pair of parallell unit-cell edges should contract, another pair should elongate, while the angle between them should change from $90°$ to $94.1°$. There are two possible choices that achieve this, and these choices can be illustrated by two choices of direction in the tetragonal cell. The two choices are crystallographically identical, and related through the fourfold rotation symmetry of the tetraconal system. In figure 2.6 the transition from the tetragonal system with point group $4/m$ (top) to the monoclinic system with point group $2/m$ (bottom) is illustrated.

These monoclinic structures are the two allowed *orientation states* of the ferroelastic phase of $LaNbO_4$ as discussed in section 2.2.

If we apply the definitions given in section 2.2, it is clear that we are dealing with the point groups:

$$L_p = \{4, m\} \qquad L_f = \{2, m\}$$

Bearing in mind that the complement of the intersection of these two point groups is denoted F, we have:

$$F = \{4\}$$

since the twofold rotation symmetry is contained in the fourfold rotation.

This indicates that we are dealing with the ferroelastic transition $4/mF2/m$ using the notation of Aizu.

Since F contains only the fourfold rotation, we see that the two OS are indeed related through a rotation of 90° as we have already argued.

It is important to realize that it is the *strain tensors* (both normal and spontaneous) that are related through the operations of symmetry contained in F. One might think that this also leads to the crystal *structures* being related by these operations, but this is generally not the case. In the case of $LaNbO_4$ it has been reported that the crystal structure of the two domains are related through a rotation about the $[010]$ axis approximately equal to β [6], [7].

2.3.2 Calculation of strain tensors

Schlenker et al. [12] have shown how we can calculate the elements of the strain tensor for a crystal based on the cell parameters. In the case of the tetragonal to monoclinic transition of $LaNbO_4$ the elements of one OS are:

$$\begin{aligned} l_{11} &= \frac{c_m \sin\beta_m^*}{a_t} - 1 \\ l_{22} &= \frac{a_m}{a_t} - 1 \\ l_{33} &= \frac{b_m}{c_t} - 1 \\ l_{12} &= -\frac{1}{2}\frac{c_m \cos\beta_m^*}{a_t} \\ l_{21} &= l_{12} \end{aligned}$$

The subscripts t and m refer to the tetragonal and monoclinic phases. The remaining tensor elements are reduced to zero by the cell parameters. See appendix A.2 for details.

The strain tensor is then:

$$\mathbf{e}(S_1) = \begin{pmatrix} l_{11} & l_{12} & 0 \\ l_{21} & l_{22} & 0 \\ 0 & 0 & l_{33} \end{pmatrix} \tag{2.3}$$

In order to find the spontaneous strain characterizing the two states, we also need to know the strain tensor $\mathbf{e}(S_2)$. We can obtain this tensor by performing a fourfold rotation about the z-axis. This is achieved by the following operation, see appendix A.1 for a detailed discussion:

$$\mathbf{e}(S_2) = \mathbf{R}\mathbf{e}(S_1)\mathbf{R}^T$$

where $\mathbf{R}$ and $\mathbf{R}^T$ are the 90° rotation matrix about the z-axis and its transpose, given by

$$\mathbf{R} = \begin{pmatrix} \cos\theta & -\sin\theta & 0 \\ \sin\theta & \cos\theta & 0 \\ 0 & 0 & 1 \end{pmatrix} = \begin{pmatrix} 0 & -1 & 0 \\ 1 & 0 & 0 \\ 0 & 0 & 1 \end{pmatrix}$$

and

$$\mathbf{R}^T = \begin{pmatrix} 0 & 1 & 0 \\ -1 & 0 & 0 \\ 0 & 0 & 1 \end{pmatrix}$$

Based on this we find the strain tensor for the second orientation state:

$$\begin{aligned} \mathbf{e}(S_2) &= \mathbf{R}\mathbf{e}(S_1)\mathbf{R}^T \\ &= \begin{pmatrix} 0 & -1 & 0 \\ 1 & 0 & 0 \\ 0 & 0 & 1 \end{pmatrix} \begin{pmatrix} l_{11} & l_{12} & 0 \\ l_{21} & l_{22} & 0 \\ 0 & 0 & l_{33} \end{pmatrix} \begin{pmatrix} 0 & 1 & 0 \\ -1 & 0 & 0 \\ 0 & 0 & 1 \end{pmatrix} \\ &= \begin{pmatrix} l_{22} & -l_{12} & 0 \\ -l_{12} & l_{11} & 0 \\ 0 & 0 & l_{33} \end{pmatrix} \end{aligned} \tag{2.4}$$

We now have all the needed elements to calculate the spontaneous strain tensors from equation (2.1):

$$\begin{aligned} \mathbf{e}_s(S_1) &= \mathbf{e}(S_1) - \frac{1}{2}[\mathbf{e}(S_1) + \mathbf{e}(S_2)] \\ &= \begin{pmatrix} l_{11} & l_{12} & 0 \\ l_{21} & l_{22} & 0 \\ 0 & 0 & l_{33} \end{pmatrix} - \frac{1}{2} \begin{pmatrix} l_{11} & l_{12} & 0 \\ l_{21} & l_{22} & 0 \\ 0 & 0 & l_{33} \end{pmatrix} - \frac{1}{2} \begin{pmatrix} l_{22} & -l_{12} & 0 \\ -l_{12} & l_{11} & 0 \\ 0 & 0 & l_{33} \end{pmatrix} \\ &= \begin{pmatrix} u & v & 0 \\ v & -u & 0 \\ 0 & 0 & 0 \end{pmatrix} \end{aligned} \tag{2.5}$$

and

$$\mathbf{e}_s(S_2) = \begin{pmatrix} -u & -v & 0 \\ -v & u & 0 \\ 0 & 0 & 0 \end{pmatrix} \tag{2.6}$$

Where $u = \frac{1}{2}(l_{22} - l_{11})$ and $v = l_{11}$. These are the same results presented by Aizu [9] and Jian and Wayman [7], experimental values for the parameters u and v can be found in the latter paper.

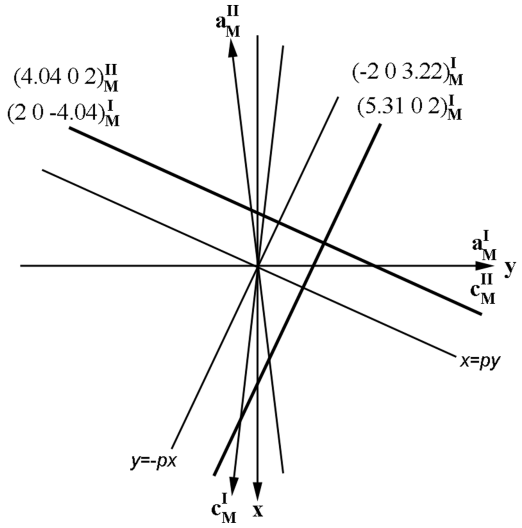

Figure 2.7: Illustration of the boundary orientations proposed by Jian and Wayman [7].

2.3.3 The domain boundary

Much attention has been given to the interface between two adjacent domains and the orientation of the domain walls. This defect has often been referred to as a *type III mechanical twin* [6]. We will interchangeably refer to these defects as both twins and domains.

As previously mentioned, Sapriel has determined the domain-wall equations for the ferroelastic species [11]. For an explicit calculation for the $LaNbO_4$-system see Jian and Wayman [7]. The domain-wall equations given by Sapriel and Jian and Wayman predict that there are two permissible orientations of the walls:

$$x = py \qquad \text{and} \qquad x = -\frac{1}{p}y \tag{2.7}$$

These domain wall equations refer to a cartesian coordinate system, and p is an experimental parameter calculated from the crystal parameters via the strain tensor (see Jian and Wayman).

Jian and Wayman have furthermore obtained values of p at various temperatures, and calculated the permissible domain-wall orientations at room temperature. These are parallel with the $(2\ 0\ \overline{4.04})_I/(4.04\ 0\ 2)_{II}$ and $(5.31\ 0\ 2)_I/(\bar{2}\ 0\ 3.22)_{II}$ planes given in the monoclinic coordinate systems of the two orientation states. The predicted planes are illustrated in figure 2.7.

Jian and Wayman claim that these results are in good agreement with the TEM studies they have performed. Other studies, however, have found the domain boundary to lie parallel to the $(2\ 0\ \overline{5.1})/(5.1\ 0\ 2)$ planes, see Tsunekawa and Takei [6]. We expect the orientation of the domain boundary to be very sensitive to the exact lattice parameters of the monoclinic phase.

There also seems to be some controversy about the nature of the transition from one domain to another. Tsunekawa and Takei [6] suggest a sharp domain boundary, while Jian and Wayman [7] claim to have observed a transition region of about 25 Å where the lattice planes bend to accommodate the change in

orientation. The latter model is illustrated in figure 2.8.

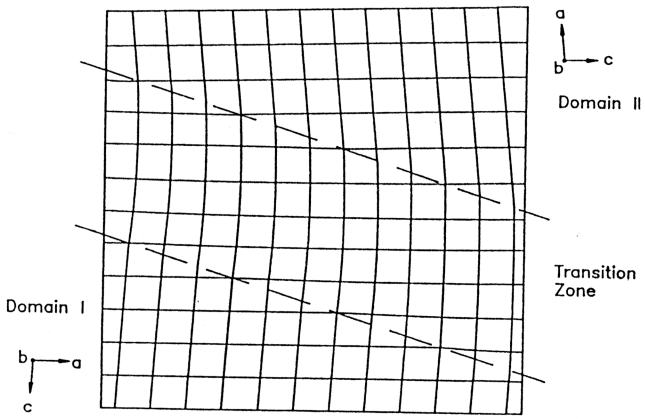

Figure 2.8: Model of the transitional region proposed by Jian and Wayman [7].

2.4 The $LaNbO_4$ system doped with Strontium

To increase the material's ion-conductivity we wish to introduce vacancies on the oxygen sites in the lattice. The undoped system is electrically neutral, this can be seen by considering the valence of the individual elements:

$$La^{3+}Nb^{5+}O_4^{2-}$$

By replacing some of the lanthanum with strontium, this balance is upset. Strontium contributes only two electrons compared to lanthanum which contributes three. The system is now running the risk of becoming electrically charged. To avoid this, vacancies on the oxygen sites are created:

$$La_{1-\delta}^{3+}Sr_{\delta}^{2+}Nb^{5+}O_{4-\delta/2}^{2-}$$

With a 5% doping with strontium, that is $\delta = 0.05$, we would expect vacancies on approximately 0.625% of the oxygen sites.

2.4.1 The bond-valence model

The bond-valence model is an empirical approach to predicting the ideal bond lengths between cations and anions. A short summary is given here, interested readers should refer to Brown [16] for an in-depth review.

The bond valence, s_{ij}, of a bond is defined through the two equations:

$$\sum_j s_{ij} = V_i \tag{2.8}$$

$$\sum_{loop} s_{ij} = 0 \tag{2.9}$$

The subscripts, i and j, refer to different atoms, and V_i is the atomic valence of atom i. The first equation states that the atomic valence of an atom i is distributed amongst the bonds with the surrounding atoms j. The second equation states that the bonds are directed, and that the bond valence is distrubuted equally in all directions. Together these conditions ensure that an atom shares its atomic valence as equally as possible among the bonds that it forms.

What makes the bond-valence model especially useful is the correlation between the bond valence and the bond length, R_{ij}. This correlation is given by Brown [16] as:

$$s_{ij} = exp\left(\frac{R_0 - R_{ij}}{B}\right) \tag{2.10}$$

Here R_0 and B are empirical parameters that must be fitted. Brown and Altermatt [17] have reported values of R_0 for many common bonds, and have shown that B can be set equal to 0.37 Å for most bonds.

From equation (2.10) we can predict the the bond lenght for two elements as:

$$R_{ij} = R_0 - B \cdot ln(s_{ij}) \tag{2.11}$$

2.4.2 Application of the bond-valence model to $LaNbO_4$ doped with Sr

The bond-valence model may give us important indications of which lattice-sites the introduced Sr will prefer.

Consider a system consisting only of a lanthanum atom with eight surrounding oxygen atoms. By using equation (2.11) we can calculate the ideal bond length of this system.

$$R_{La-O} = 2.172 \text{ Å} - 0.37 \text{ Å} \cdot ln(\frac{3}{8}) = 2.53 \text{ Å}$$

Here we have used the parameters R_0 and B provided by Brown and Altermatt [17]. The atomic valence of lanthanum is 3, divided amongst the eigth bonds to the surrounding oxygen atoms, gives the argument $\frac{3}{8}$ of the logarithm.

Applying the same procedure to a system consisting of a niobium atom surrounded by eight oxygen atoms yields:

$$R_{Nb-O} = 2.08 \text{ Å}$$

We now wish to substitute one of these cations with a strontium atom. The ideal bond length of a strontium atom surrounded by eight oxygen atoms is:

$$R_{Sr-O} = 2.63 \text{ Å}$$

These calculations indicate that introducing Sr atoms on any of the metal sites will strain the crystal lattice, thereby raising the lattice energy. We note, however, that the ideal bond length for the $La - O$ system is only slightly less than the ideal bond length for the $Sr - O$. This suggests that it may be energetically favourable for the Sr atoms to occupy the La-sites instead of the Nb-sites. The complications associated with introduction of oxygen-vacancies caused by the lower valence of Sr compared to La has not been considered.

Chapter 3

Specimen preparation and experimental techniques

3.1 Specimen preparation

Nominally 5% Sr doped $LaNbO_4$ samples were produced by cold crucible induction melting and supplied by dr. Yurii M. Baikov of the Ioffe Institute of St. Petersberg within the framework of INTAS-project no. 99-0636.

TEM specimens were prepared in two ways:

1. Samples were ground in acetone in an agate mortar and deposited on a copper mesh.
2. Samples were mechanically polished before thinning in a Gatan Precision Ion Polishing System with twin argon-ion guns. A 4 kV gun voltage was used, and the beam was oriented at 8° relative to the specimen surface, see figure 3.1. Under these conditions approximately three hours of milling were needed to thin the specimens adequately.

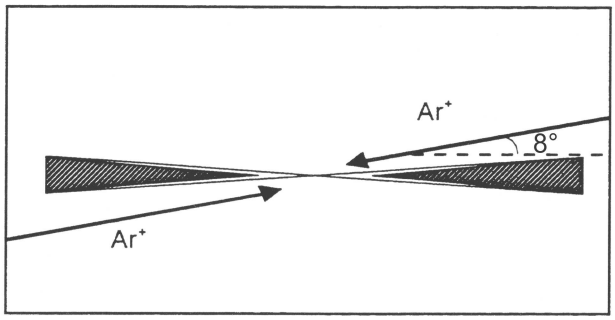

Figure 3.1: Sketch of a cross section of the TEM specimen during ion milling. Adapted from [18].

3.2 Scanning electron microscopy

The surface of the bulk samples received were studied in a Philips XL30 scanning electron microscope fitted with an EDAX EDS detector. Quantitative EDS analyses were performed using the PVSUPQ routine of the EDAX PV9900 software.

3.3 Transmission electron microscopy

A JEOL 2000FX transmission electron microscope (TEM) fitted with a Tracor Northern X-ray detector with a SCANDNORAX EDX-analyser was used to perform the bright field, diffraction and compositional studies unless otherwise noted. A JEOL 2010F fitted with a Noran Pioneer X-ray detector was used for high resolution electron microscopy and compositional studies of the domain boundaries. Both microscopes were operated at 200 kV.

During high resolution electron microscopy (HREM), the sample is illuminated with parallel electron beams. In principle, all electrons participate in forming the image, and electrons scattered from one point in the sample are focussed in one point in the image plane, see figure 3.2.

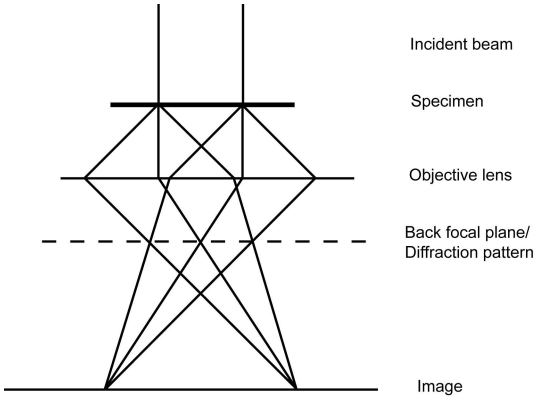

Figure 3.2: Ray diagram illustrating HREM imaging and diffraction.

A thin specimen in a microscope with perfect lenses would produce an image with very little contrast. A higher degree of contrast can be obatined by bright field (BF) or dark field (DF) imaging. These techniques involve placing an aperture in the back focal plane to remove some electrons from imaging. In BF, only electrons scattered in the forward direction are used to create the image, see figure 3.3. In DF, only electrons scattered in specific direction other than the forward direction are used to create the image.

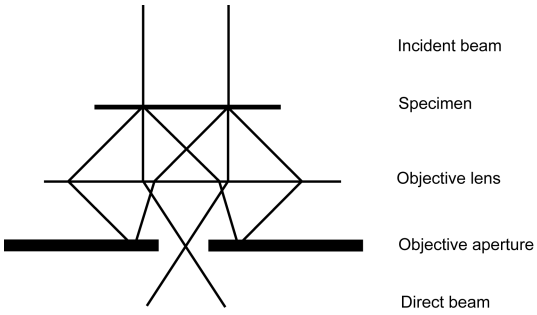

Figure 3.3: During bright field imaging, only electrons that are scattered in the forward direction are allowed to create the image.

3.4 Diffraction studies

Selected area diffraction (SAD) was used to study the crystal structure of the samples. In SAD, the sample is irridated with parallel electron beams. Electrons scattered in the same direction are then focussed to the same point in the back focal plane, giving rise to a diffraction pattern, see figure 3.2. This diffraction pattern is approximately a plane in the reciprocal lattice of the crystal being studied. An aperture is inserted in the image plane of the objective lens to obtain a diffraction pattern from a specifc region of the sample. Most SAD studies were done with at camera length $L = 0.68$ m.

3.4.1 The effect of domain boundaries on electron diffraction

When we cross from one domain to another with different crystallographic orientation, equivalent planes will lie in different directions. As a consequence, the directions of the reciprocal lattice vectors will be different on the two sides of the domain boundary.

The result will be two identical reciprocal lattices with different orientations. A diffraction pattern obtained from both sides of a domain boundary will reveal both lattices. Figure 3.4 shows an example of the effect of two twinned domains on the reciprocal lattice.

We see the presence of the two domains as a splitting of the reciprocal lattice. The intensity of the different reflections depend, as usual, on the structure factor of the crystal, but also on how big a volume on either side of the boundary is illuminated by the incident electron beam.

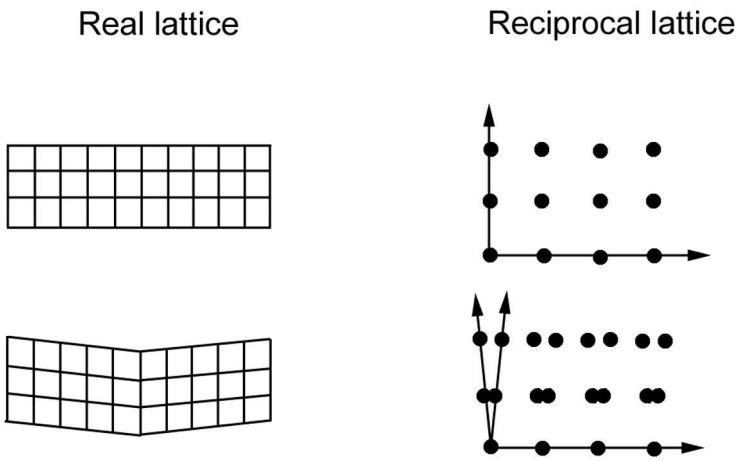

Figure 3.4: The effect of twinning on the reciprocal lattice (adapted from Olsen [19]).

3.5 Studies of compostition

A quantitative analysis of the concentration, C, of the various elements can be done based on the the X-ray spectra obtained in the TEM, and the Cliff-Lorimer equation:

$$\frac{C_1}{C_2} = \frac{k_{1,Si} \cdot I_1}{k_{2,Si} \cdot I_2} \tag{3.1}$$

Here I_1 and I_2 are the intensities of the peaks of two elements, while $k_{1,Si}$ and $k_{,Si}2$ are the k-factors of the elements relative to silicon. The k-factors are a measure of the rate at which an element produces characteristic radiation when irridated with electrons. All element have a different k-factor for each peak of the characteristic radiation. Furthermore the k-factors take different values depending on the equipment used to obtain the spectra and the acceleration voltage used in the microscope. Values of k for the different elements for the 2000FX microscope have been reported by Olsen [19], see table 3.1.

Table 3.1: k-factors relative to Si for the L- and K-lines of Sr, Nb and La. Obtained for the JEOL 2000FX microscope at 200kV [19].

Element	L	K
Sr	$k = 1.10$	$k = 0.77$
Nb	$k = 0.86$	$k = 0.89$
La	$k = 0.55$	$k = 4.46$

Chapter 4

Results and interpretation

4.1 Studies of composition and structure

4.1.1 Preliminary studies of composition

The bulk sample received from Russia was nominally 5% Sr-doped $LaNbO_4$. We performed som introductory analyses to check the validity of this claim.

SEM studies The bulk sample received from Russia was studied in the scanning electron microscope.

When using the back-scattered electron (BSE) detector, the sample exhibits areas of different shading, indicating that the intensity of backscattered electrons varies spatially. This can be the result of many factors, but may indicate that the compsition of the sample is inhomogeneous. Figure 4.1(a) shows a typical SEM image obtained by detecting the backscattered electrons.

EDS spectra collected at various positions of the surface seem to confirm that there are at least two phases present in the sample: one with a low Sr content, and one with a higher percentage of Sr. Figure 4.1(b) indicates two positions whose corresponding spectra are presented in closer detail in figure 4.2.

The two spectra indicate that there is a higher concentration of Sr at position B than there is at position A, suggesting that they indeed are two different phases. A quantitative analysis of the two spectra was performed, indicating the relative amounts of the various elements. The results are presented in table 4.1, and confirm a higher concentration of Sr at position B. The accuracy of these results should not be overestimated, but rather seen as a confirmation of the presence of different phases.

Even though the aim was to synthesize a single phase sample containing 5% Sr, there is good reason to believe that it has segregated into at least two phases with different composition.

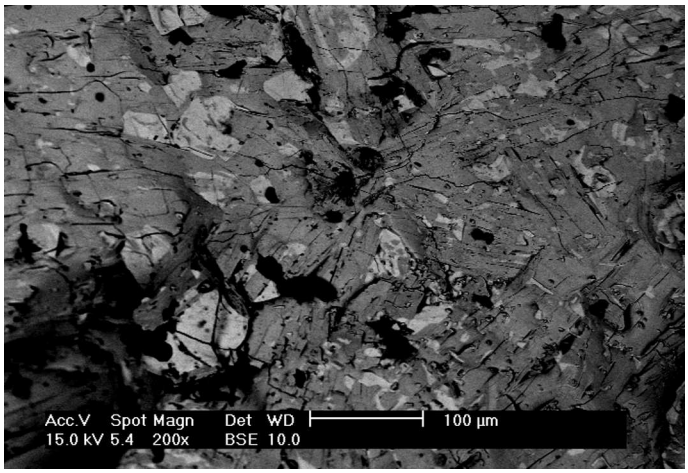

(a) Typical surface structure of the bulk Russian sample. Notice the differences in shading of different areas.

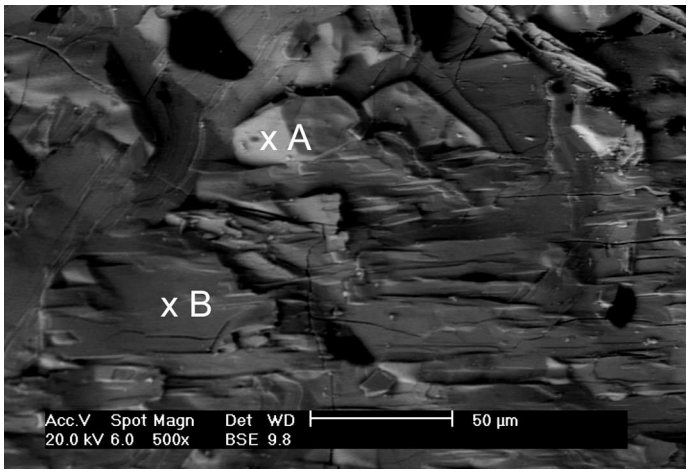

(b) An EDS analysis was performed at the locations marked A and B.

Figure 4.1: Two images of the surface of the russian bulk sample obtained by detecting the backscattered electrons.

Table 4.1: Concentration of metals at two positions of the Russian sample.

	Element	Concentration not corrected for absorbtion	Concentration corrected for absorbtion
Position A	Sr	2.3%	1.5%
	Nb	50.0%	57.4%
	La	47.7%	41.1%
Position B	Sr	11.2%	7.2%
	Nb	62.0%	70.3%
	La	26.0%	22.5%

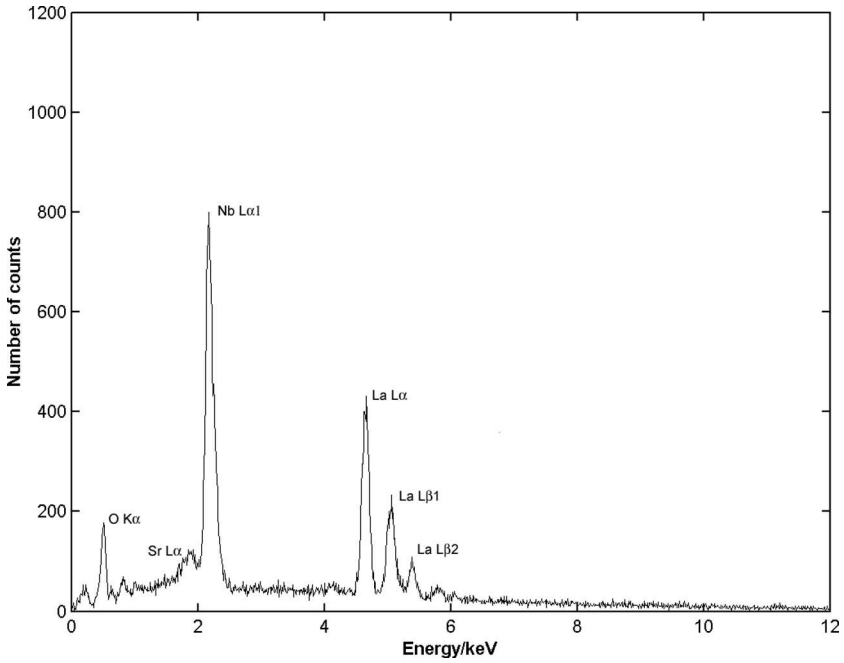

(a) The spectrum obtained from position A.

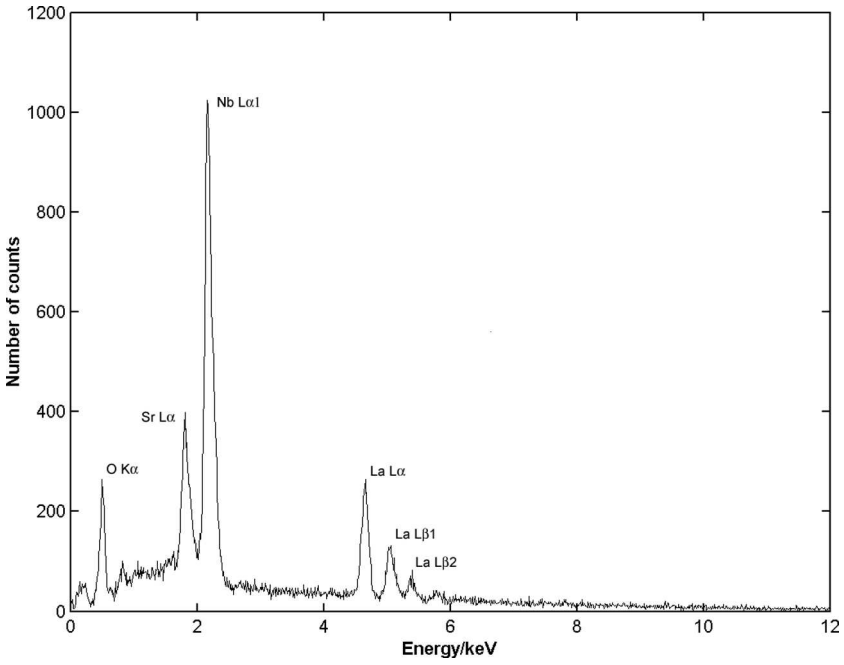

(b) The spectrum obtained from position B.

Figure 4.2: The spectra obatined from positions A and B of the bulk surface. Notice that postition B displays a much more prominent Sr Lα line than position A.

EDS using TEM As we have seen evidence of more than one phase in the sample, we performed EDS analyses in the TEM to identify these phases. These EDS analyses confirm that there are two distinctly different phases present. The spectra of the two phases are presented in figure 4.3(a) and 4.3(b).

Calculations using the Cliff-Lorimer equation (3.1) reveal that the La-rich phase has approximately a one–to–one ratio between La and Nb, consistent with $LaNbO_4$, see figure 4.3(a). The Sr content of this phase has been calculated to be approximately 2.9%. We expect that this value is somewhat high due to contamination from adjacent Sr-rich grains during the analysis, and that the actual amount of Sr is somewhat less.

There is uncertainty as to the exact composition of the Sr-rich phase (figure 4.3(b)), our calculations suggest a Sr:Nb ratio between 1:2 and 1:3. There is also some evidence of La in this phase, but it is difficult to determine how much of this is due to contamination of the spectrum from adajcent La-rich grains.

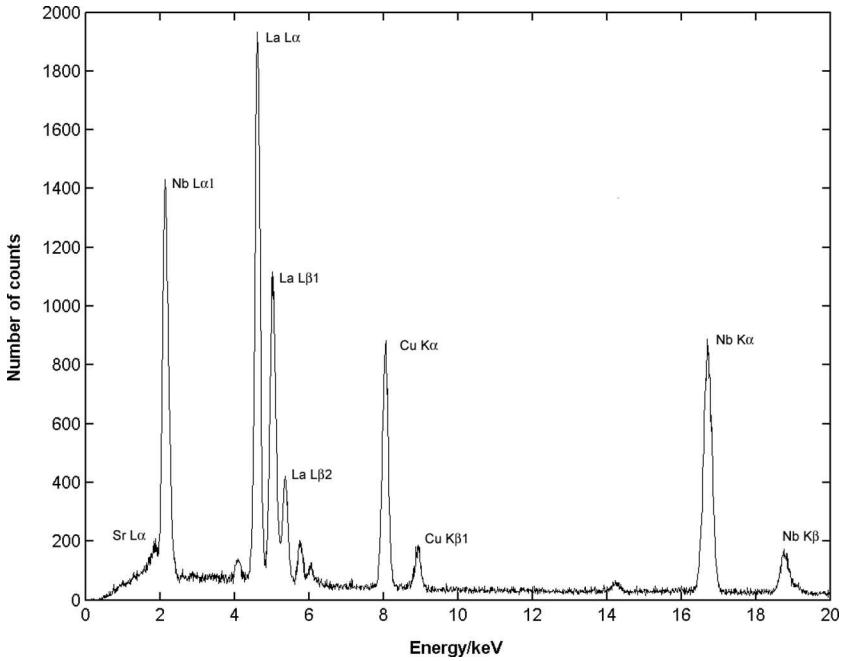

(a) The EDS spectrum obtained from a La-rich grain.

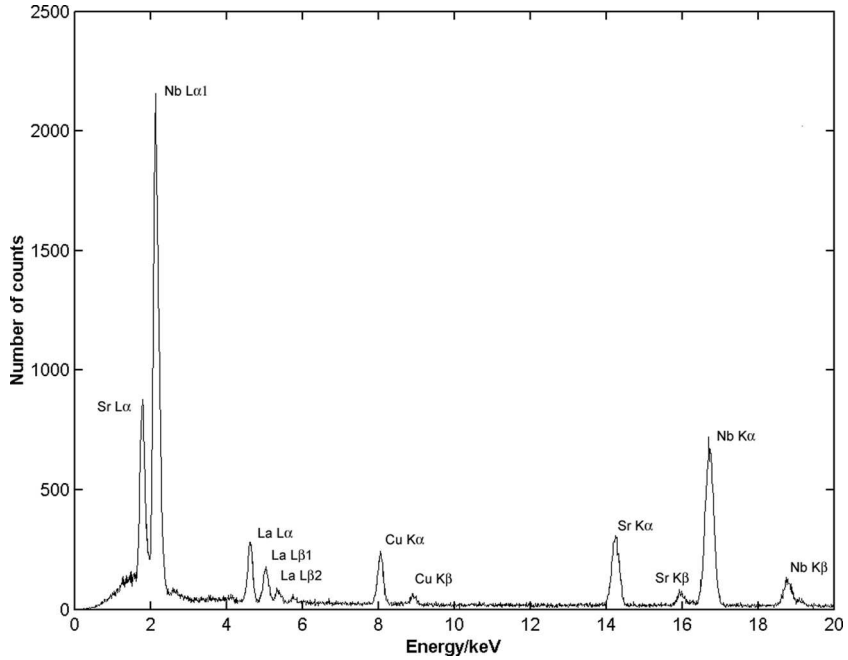

(b) The EDS spectrum obtained from a Sr-rich grain.

Figure 4.3: SPectro from the La-rich and Sr-rich phases obtained in the 2000FX.

4.1.2 The structure of the Sr-rich phase

To identify the structure of the Sr-rich phase we performed selected area diffraction studies in the JEOL 2000FX microscope. There is a clear orientation preference in our samples, making the study of some projections difficult.

Our SAD studies have revealed an axis with very small spacing between reflections, as seen in figure 4.4(b). We dub this the $\mathbf{c}^*$ axis, and refer to the projection seen in figure 4.4(b) as $[100]$. We have revealed no significant deviation from 90° between the $\mathbf{b}^*$ and $\mathbf{c}^*$ axes, and conclude that $\alpha = 90^\circ$.

Tilting the sample either way about the $\mathbf{c}^*$ axis, we observe the $[310]$ and $[3\bar{1}0]$ projections, see figures 4.4(a) and 4.4(c). These projections reveal a symmetry about the $\mathbf{c}^*$ axis, for example we observe that $d_{\bar{1}30} = d_{130}$. This suggests that the $\mathbf{a}^*$ and $\mathbf{b}^*$ axes are orthogonal, i.e. $\gamma = 90^\circ$. The plane distances in table 4.2 were obtained in a tilt-series about the $\mathbf{c}^*$ axis, figure 4.8, and about the $\mathbf{b}^*$ axis, figure 4.6.

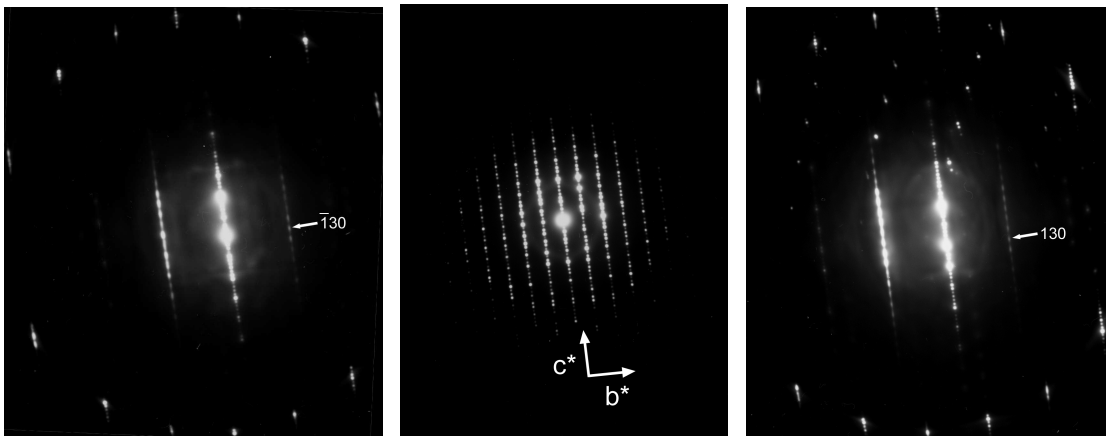

(a) SAD pattern from the $[310]$ projection of Sr-rich phase.

(b) SAD pattern from the $[100]$ projection of Sr-rich phase.

(c) SAD pattern from the $[3\bar{1}0]$ projection of Sr-rich phase.

Figure 4.4: SAD images from the Sr rich phase.

Table 4.2: Experimental d-values in the Sr rich phase.

Plane	d_{exp}/Å
(001)	30.75
(103)	6.65
(010)	5.81
(105)	4.82
(110)	4.74
(210)	3.27
$(\bar{1}20)$	2.71
(120)	2.70
(410)	1.91
$(\bar{1}30)$	1.86
(130)	1.86
(230)	1.76

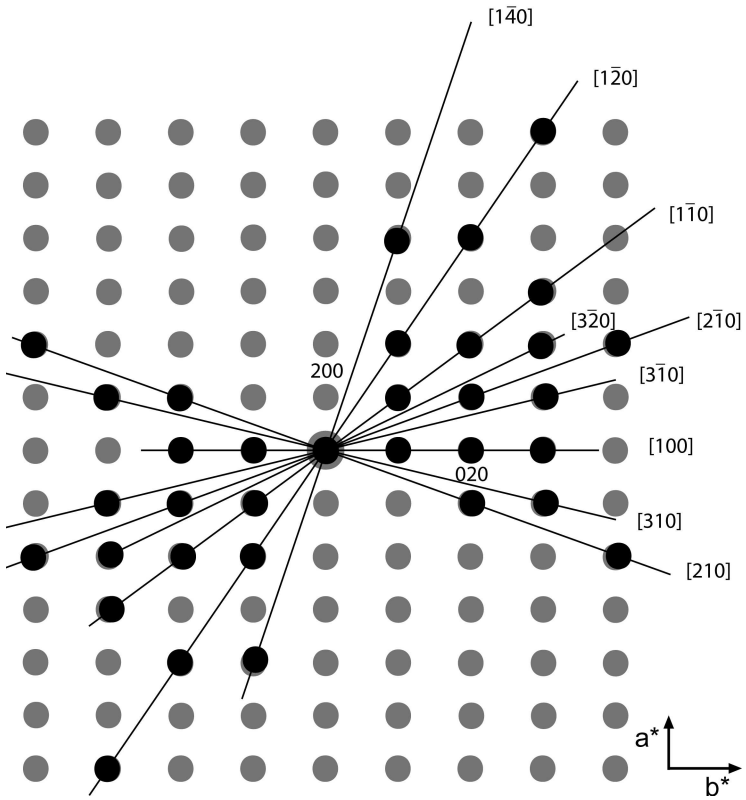

Figure 4.5: Sketch illustrating our observations, and an idealized lattice based on these, seen in the $[001]$ projection. The observations are drawn in black, and the ideal lattice in grey. The projections in which the observations were done are indicated to the right.

The $[001]$ projection has not been observed, but the observations from tilting the sample about the $\mathbf{c}^*$ axis allows us to map parts of this projection. Figure 4.5 illustrates our observations seen in the $[001]$ projection together with an idealized generalization of the lattice. In this projection, the idealized lattice is rectangular with edges corresponding in real space to $b = 5.81$Å which has been observed directly, and $a = 7.91$Å which was obtained by fitting to the observed plane distances.

Tilting the sample about the $\mathbf{b}^*$ axis allows us to investigate other parts of the reciprocal lattice. Only two such projections were studied, the DPs from these projections are shown in figure 4.6. Figure 4.7 shows a map of the $[010]$ projection, here the idealized lattice is based on the value for a obtained in the previous tilt-series, direct observations of the $\mathbf{c}^*$ axis and we have assumed $\beta = 90°$.

The two projections observed when tilting about the $\mathbf{b}^*$ axis are in good agreement with the previous tilt-series under the assumption that $\beta = 90°$. However, further studies are needed to determine the true value of this angle. Our observations of the Sr-rich phase are consistent with a monoclinic or orthorhombic structure with cell parameter $a = 7.91$Å, $b = 5.81$Å and $c = 30.75$Å.

When tilting about the $\mathbf{c}^*$ axis, we observe diffuse scattering in some reflections, see figure 4.8. The diffuse scattering appears for all indices $hkl : h = 2n + 1$ and are directed along the $\mathbf{c}^*$ axis. However, diffuse scattering is not observed when tilting about the $\mathbf{b}^*$ axis, see figure 4.6, indicating that there is no diffuse scattering in this direction. We have seen no evidence of diffuse scattering in the $\mathbf{a}^*$ direction.

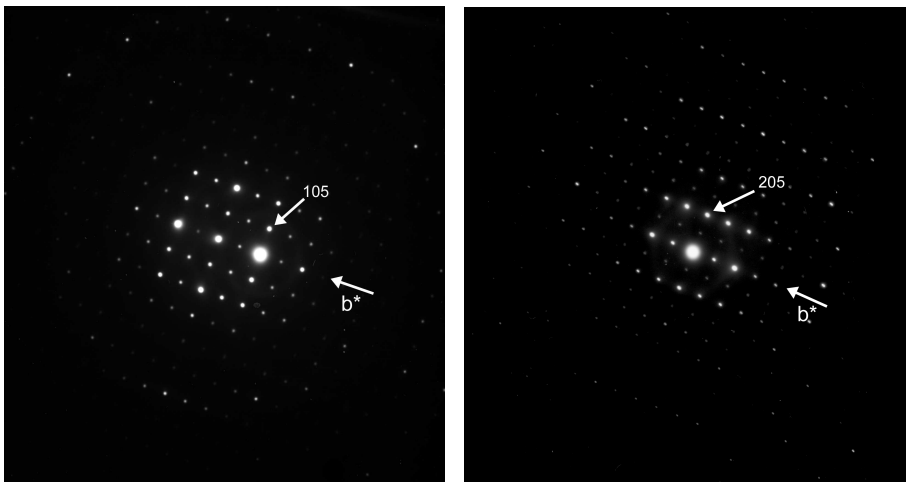

(a) SAD pattern from the $[\bar{5}01]$ projection of Sr-rich phase.

(b) SAD pattern from the $[\bar{8}01]$ projection of Sr-rich phase.

Figure 4.6: SAD images from the Sr rich phase.

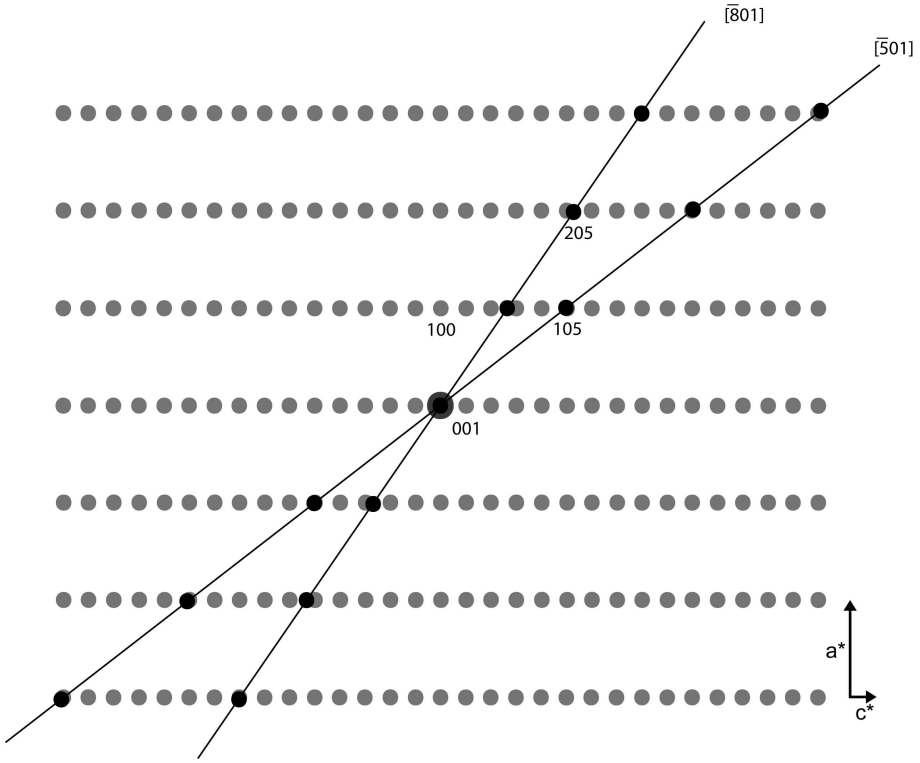

Figure 4.7: Sketch illustrating our observations and an idealized lattice seen in the $[010]$ projection. The observations are drawn in black, and the ideal lattice in grey.

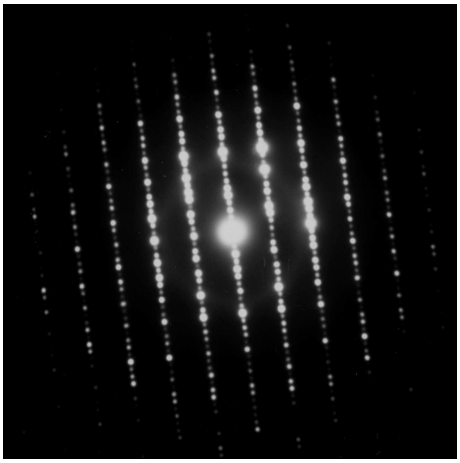

(a) The $[100]$ projection.

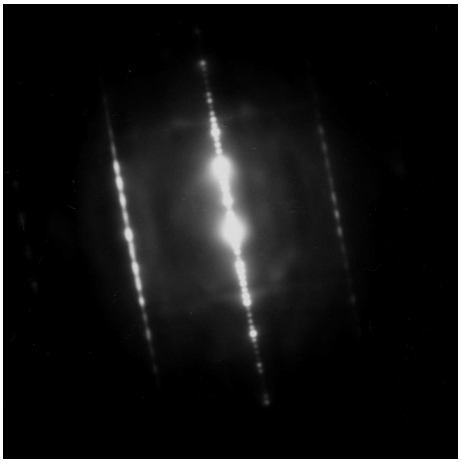

(b) The $[3\bar{1}0]$ projection.

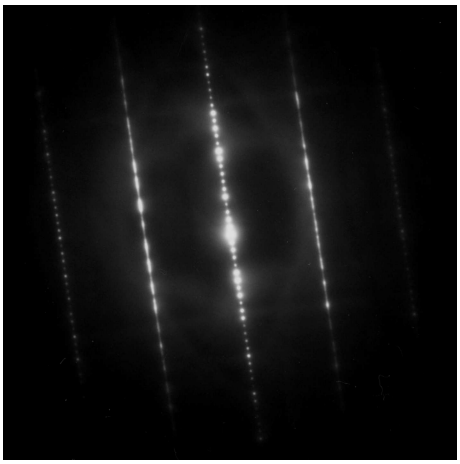

(c) The $[2\bar{1}0]$ projection.

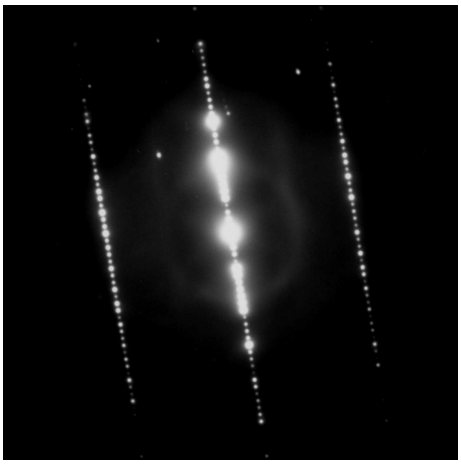

(d) The $[3\bar{2}0]$ projection.

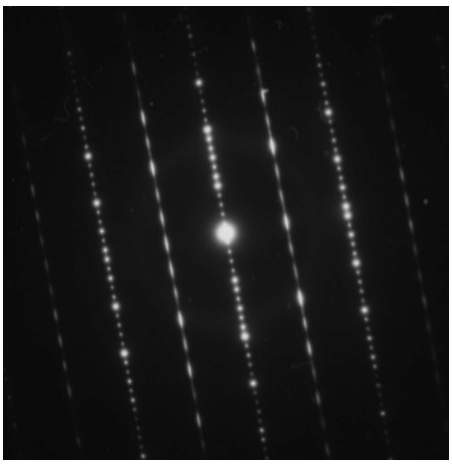

(e) The $[1\bar{1}0]$ projection.

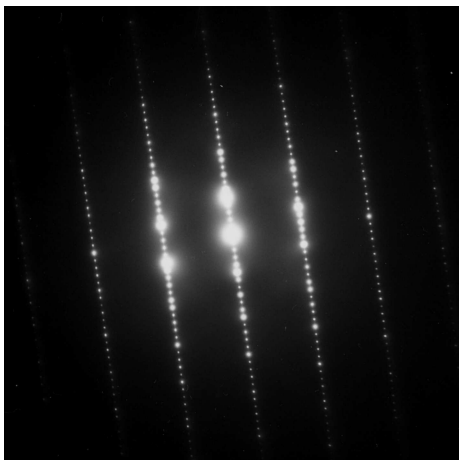

(f) The $[1\bar{2}0]$ projection.

Figure 4.8: Six DPs showing diffuse scattering. The direction with densely spaced reflections is the $\mathbf{c}^*$ direction.

4.1.3 The structure of the La-rich phase

As mentioned in chapter 2.3, $LaNbO_4$ has been reported to be monoclinic at room temperature with the space group $C2/c$ [5], or $I2/c$ using a non-standard setting for easy comparison to the high-temperature phase. Much of the Sr has precipitated to a seperate phase, leaving smaller amounts in the $LaNbO_4$ than intended.

To test for the effect of Sr on the lattice parameters and crystal structure, we performed selected area diffraction (SAD) with the JEOL 2000FX microscope. Four diffraction patterns (DPs) obtained in this way are presented in figure 4.9.

The plane distances measured from these DPs closely match those corresponding to the cell dimensions given by Tsunekawa et al. [15] (these values can also bee found in ICSD, see Appendix B). The measured plane distances (d_{exp}) are listed in table 4.3 together with the values obtained by Tsunekawa et al.

These values give cell dimensions of $a = 5.55$Å, $b = 11.62$Å and $c = 5.21$Å. This is a deviation of less than 1 % from the values given by Tsunekawa et al., and well within the uncertainty of the measurements performed. The measured values of the angles α and γ show no significant deviation from the expected $90°$, while β was measured to be $94.3 \pm 0.5°$.

Table 4.3: Experimental d-values obtained in the present study, compared to d-values based on the cell parameters given by Tsunakwa et al. [15].

Figure	Plane	d_{exp}/Å	d/Å
4.9(a)	(200)	2.78	2.78
	(002)	2.60	2.59
	(202)	1.81	1.83
	$(20\bar{2})$	1.99	1.97
4.9(b)	(011)	4.76	4.73
	$(01\bar{1})$	4.79	4.73
	$(0\bar{2}0)$	5.81	5.76
	(002)	2.62	2.59
4.9(c)	(011)	4.72	4.73
	$(1\bar{1}0)$	5.00	5.00
	$(\bar{1}0\bar{1})$	3.62	3.66
4.9(d)	(011)	4.69	4.73
	$(10\bar{1})$	3.98	3.93
	$(\bar{1}\bar{2}\bar{1})$	3.05	3.09

Closer inspection of figure 4.9(c) and 4.9(d) reveal some reflections that do not fulfill the conditions for reflection imposed by space group $I2/c$ [1]. Reflections of the type $h0l$ are only allowed for $h, l = 2n$, but several reflections not obeying this rule appear in these two figures (e.g. 101 and $\bar{1}01$). The presence of these reflections could indicate that we are dealing with another space group than assumed. We note, however, that the 101 and similar reflections do not appear in figure 4.9(a). This indicates that we are *not* dealing with conditions for reflection that allow these reflections, but instead a case of double scattering causing prohibited reflections to appear in the DP.

These findings are in excellent agreement with the structure and cell parameters reported for the low-temperature phase of $LaNbO_4$. We conclude that the La-rich phase is indeed $LaNbO_4$.

[1] These are the same as for $I2/a$, see appendix B.

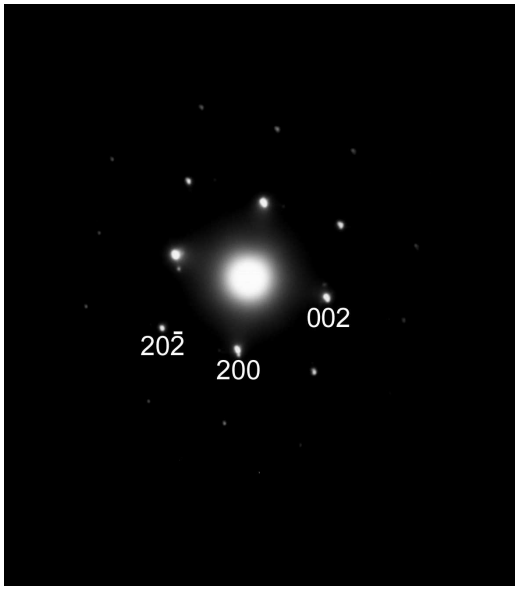

(a) The $[010]$ projection.

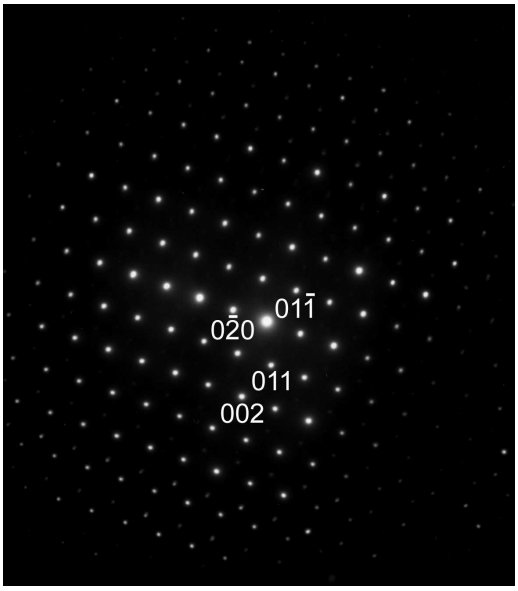

(b) The $[100]$ projection.

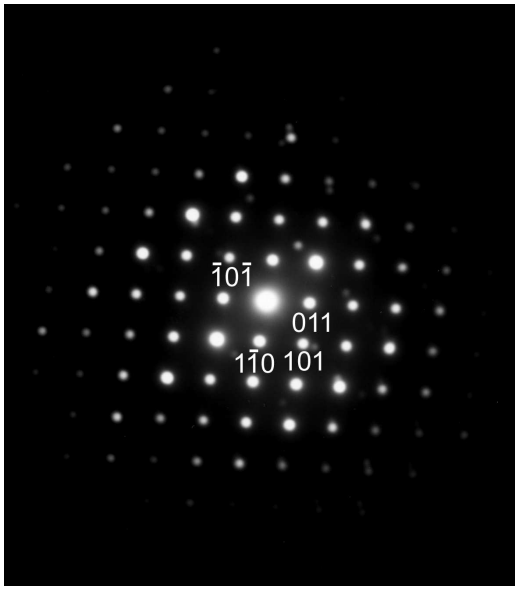

(c) The $[\bar{1}\bar{1}1]$ projection. Notice the $h0l$-type reflections not satisfying the condition $h, l = 2n$.

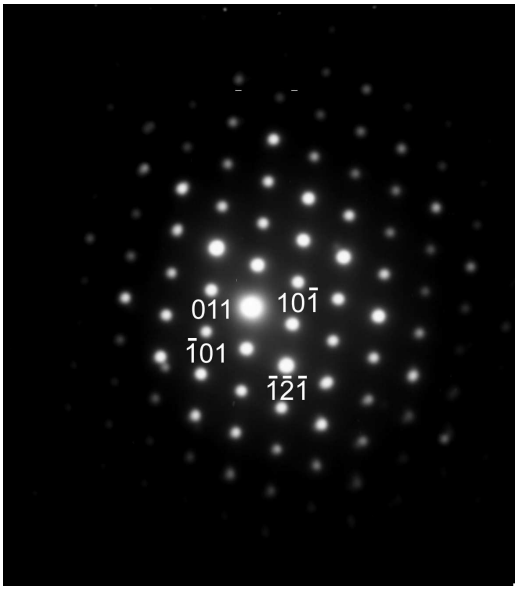

(d) The $[1\bar{1}1]$ projection. Notice the $h0l$-type reflections not satisfying the condition $h, l = 2n$.

Figure 4.9: Four different projections used to calculate the cell parameters and verify the crystal structure of the La-rich phase.

4.2 The Domain structure of $LaNbO_4$

4.2.1 Observations of domains

Our studies have revealed heavy twinning in the La-rich phase. This is consistent with the findings of Tsunekawa and Takei [6], Jian and Wayman [7] and several others for the pure $LaNbO_4$ system. We are not able to conclude whether there is more or less twinning in our Sr-doped system than in the pure $LaNbO_4$ of the mentioned studies. Figures 4.10 and 4.11 show bright field images of typical twinning structures.

The width of the domains were observed to vary from less than 20 nm, as in figure 4.11(a), to almost 300 nm as in figure 4.11(c). One may also note that the width often varies periodically, with wide and narrow domains appearing next to each other.

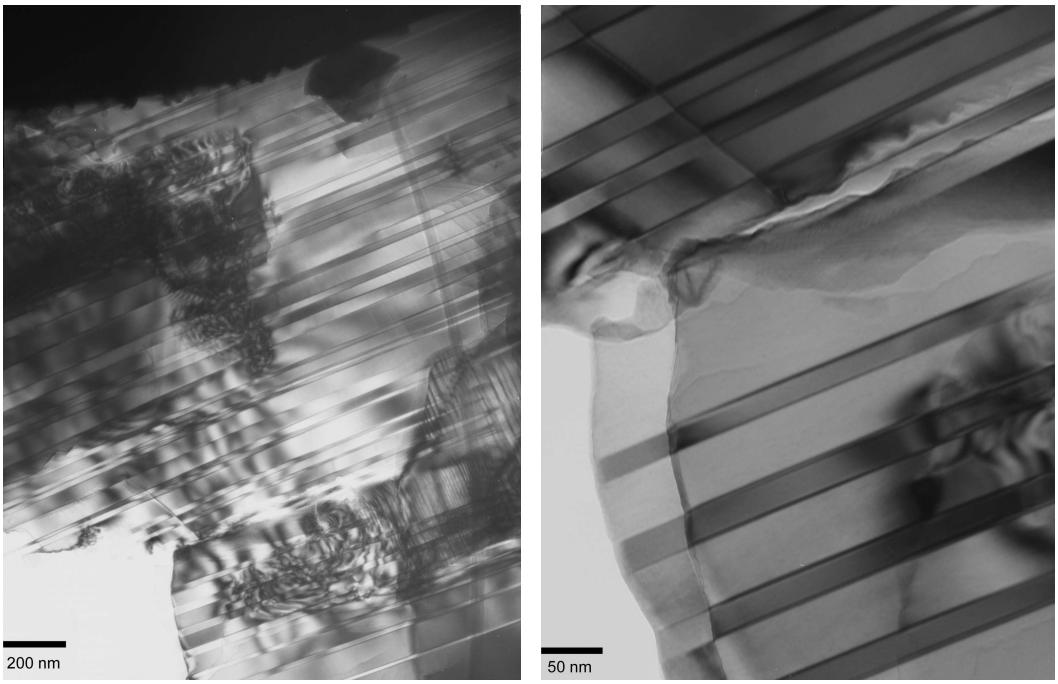

(a) Brightfield image showing a heavily twinned region of the sample.

(b) The same region as in 4.10(a) at greater magnification. Notice the alternating size of the domains.

Figure 4.10: Bright field images showing a part of the sample exhibiting an unusually high density of twinned domains.

The diffraction patterns associated with the brightfield images exhibit a splitting of most reflections in the $[010]$ projection, see figure 4.11(b) and 4.11(d). As noted in chapter 3.4.1, this indicates that we are obtaining a diffraction pattern from two domains with different lattice orientation.

A closer examination of the DPs exhibiting this kind of splitting reveals that the reciprocal lattices, and thereby the real lattices, of the two domains are related through a rotation of slightly more than 95° about the $[010]$ axis. This angle is larger than β by approximately 1°.

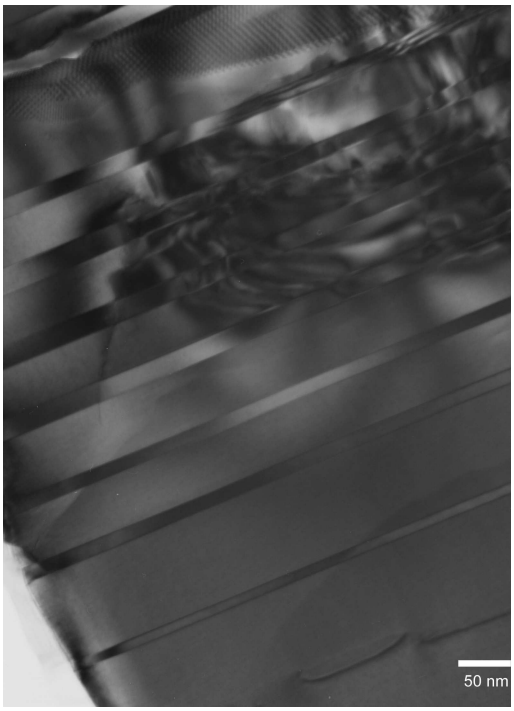

(a) Bright field image from the same region as figure 4.10.

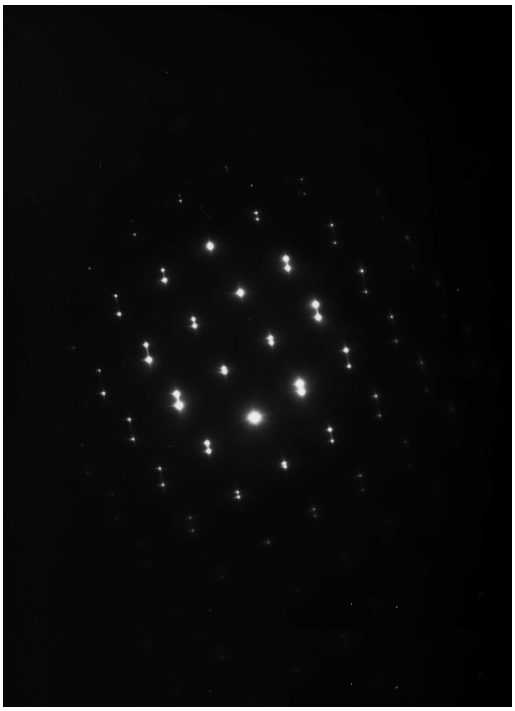

(b) DP obtained from the region seen in figure 4.11(a)

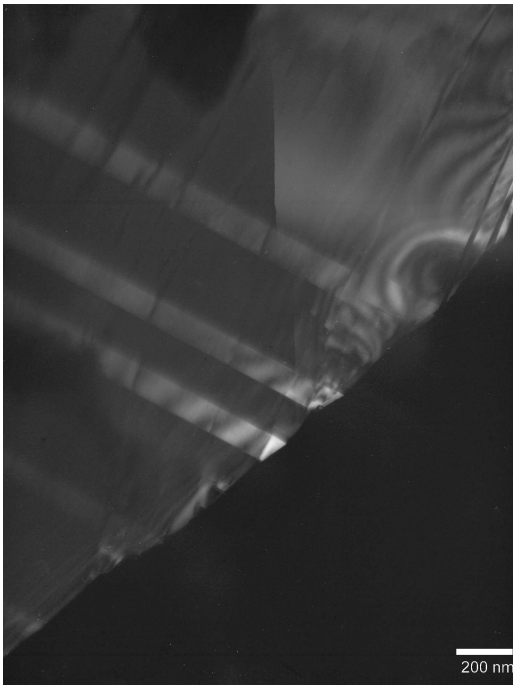

(c) Bright field image at low magnification showing large twinned domains.

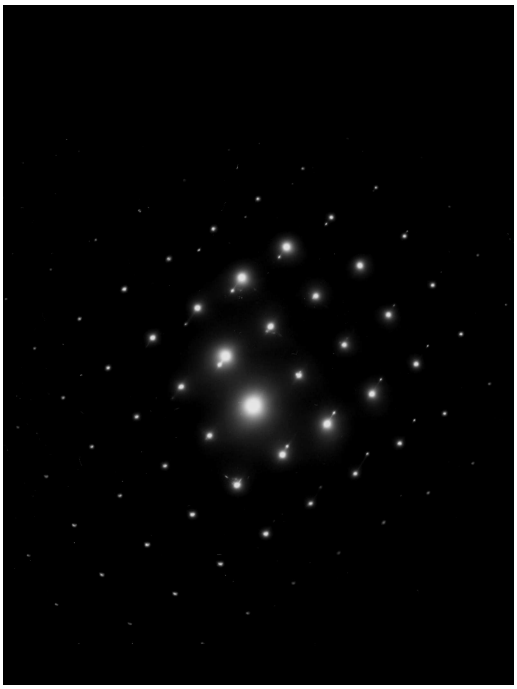

(d) DP obtained from the region seen in figure 4.11(c)

Figure 4.11: Bright field images and the related DPs in the $[010]$ projection. The splitting of reflections indicate variations in lattice orientation.

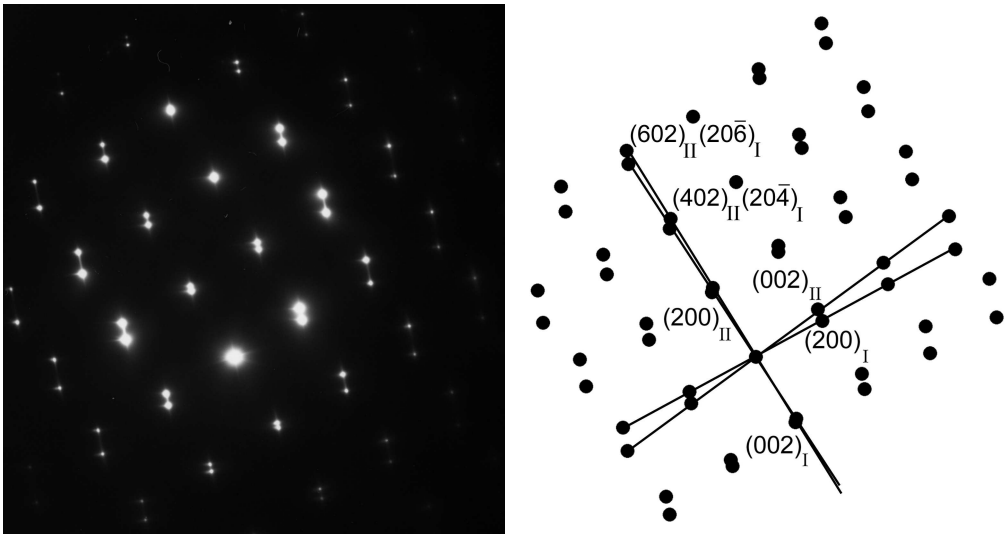

(a) Enlargement of the DP in figure 4.11(b)

(b) The index of the DP shown in (a).

Figure 4.12: Diffraction pattern form the $[010]$ projection, obtained from a twinned region and the index of the pattern. Notice that the $(20\bar{4})_I/(402)_{II}$ and $(20\bar{6})_I/(602)_{II}$ pairs seem to overlap, indicating that these planes have the same orientation in the two domains. The DP in figure (a) was obtained in the 2010F microscope.

Figure 4.12 shows a diffraction pattern from the $[010]$ projection with splitting of reflections and an index-map. We can immediatley note that the reflections corresponding to the $(20\bar{4})_I/(402)_{II}$ and $(20\bar{6})_I/(602)_{II}$ planes of the two domains seem to overlap. This indicates that these planes have the same orientation in the two domains, and that the domain boundary is closely related to these planes.

By tilting the sample somewhat out of the $[010]$ projection, we were able to observe higher-index reflections, see figure 4.13(a). We notice that there appears to be no splitting of the reflection corresponding to the $(4\ 0\ \overline{10})_I/(10\ 0\ 4)_{II}$ planes, indicating that the true orientation of the domain boundary is parallel to these planes. For easy comparison with previous results, we may instead consider the parallel planes $(20\bar{5})_I/(502)_{II}$.

In order to test whether or not there is any splitting of the $(4\ 0\ \overline{10})_I/(10\ 0\ 4)_{II}$ reflections, we consider the idealized situation sketched in figure 4.13(b). The two diffraction spots we are considering are located halfway between the neighbouring spots of their respective lattices, that is, halfway along the diagonals with length $2u$ and $2v$ as indicated in the sketch. If we assume that there is no splitting, this must be the intersect of the two diagonals as in figure 4.13(b). In this case, two sides and one angle of the triangles are equal, and we are dealing with two congruent trangles. If this is the case, the lengths d_1 and d_2 must be equal. By measuring the lenghts d_1 and d_2 we can now test the assumption that there is no splitting of the reflections.

Careful measurement of the lengths d_1 and d_2 revealed that d_2 is larger than d_1 by approximately 10%, thereby violating the requrements imposed by assuming no splitting of the reflections. From this we conclude that the boundary is almost, but not quite, parallel to the $(20\bar{5})_I/(502)_{II}$ planes.

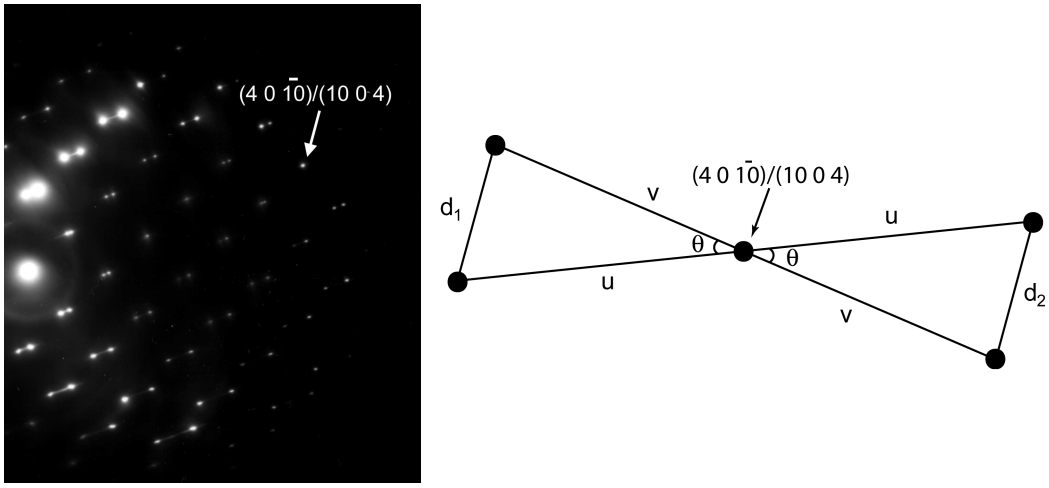

(a) SAD image tilted somewhat out of the $[010]$ projection. Notice the lack of splitting of the $(4\,0\,\overline{10})_I/(10\,0\,4)_{II}$ reflections.

(b) Sketch of the arrangement of spots in the case of no splitting.

Figure 4.13: SAD image and sketch

4.2.2 HREM study of the domain boundary

By directly observing the domain boundary it is possible to determine the nature of the transition from one domain to another. High resolution electron microscopy (HREM) allows us to do this, assuming that we view the crystal in the appropriate projection, that is the $[010]$ projection.

Figure 4.14 shows a HREM image of a domain boundary viewed approximately in the $[010]$ projection. We immediately notice that at least part of the boundary exhibits contrast similar to that which led Jian and Wayman to describe a transition region [7]. A transition zone of this kind is a region where the lattice planes presumably bend to accomodate the misfit caused by the domain boundary.

In the indicated area of figure 4.14, the width of this transition zone is approximately 15 Å. Observing the boundary closer to the edge of the grain where the sample is thinner, however, reveals a progressively more narrow transition zone.

This leads us to suspect that what we observe might not be an actual area of transition between the two domains, but rather a result of the electron beam being improperly aligned with regard to the domain boundary. If the beam is tilted slightly out of the $[010]$ projection, a planar defect cutting through the sample in this direction will be observed as a region of changed contrast, with a width depending on the sample thickness. This is consistent with our observations in figure 4.14.

By aligning the sample and electron beam properly, we were able to observe the domain boundary precisely in the $[010]$ projection. As seen in figure 4.15, there was little or no indication of a transition zone in this projection. On the contrary, our observations suggest a sharp transition from one domain to another.

It is difficult to completely dismiss the possibility of a transition zone. A very narrow zone, for example in the order of less than 10 Å, would be very difficult observe directly. In addition, the misfit between the

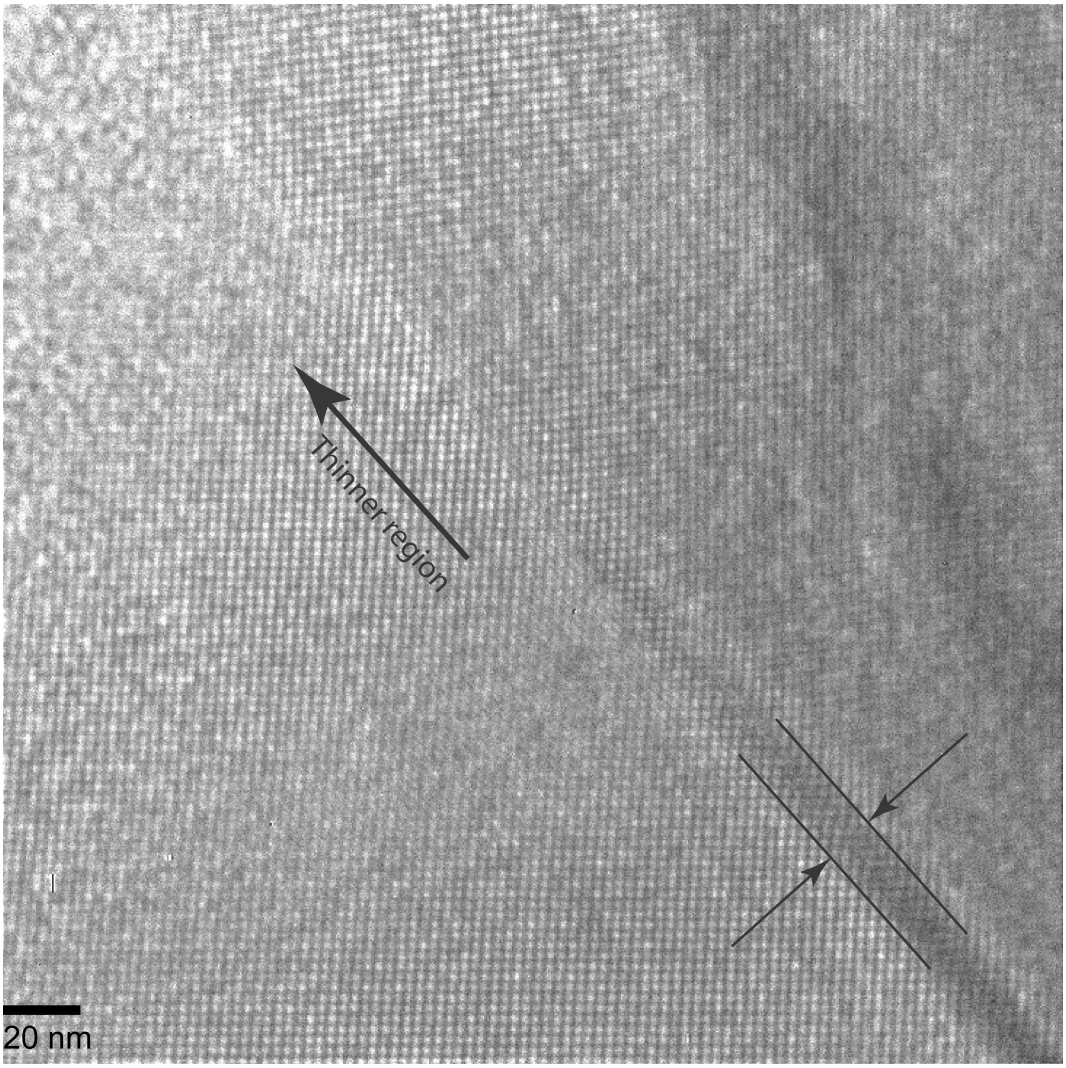

Figure 4.14: HREM image of a domain boundary exhibiting a transition zone similar to that suggested by Jian and Wayman. Notice that the transitional region becomes thinner as we move towards the edge of the sample where the thickness of the sample decreases. The transition zone is approximately 15 Å wide in the indicated region.

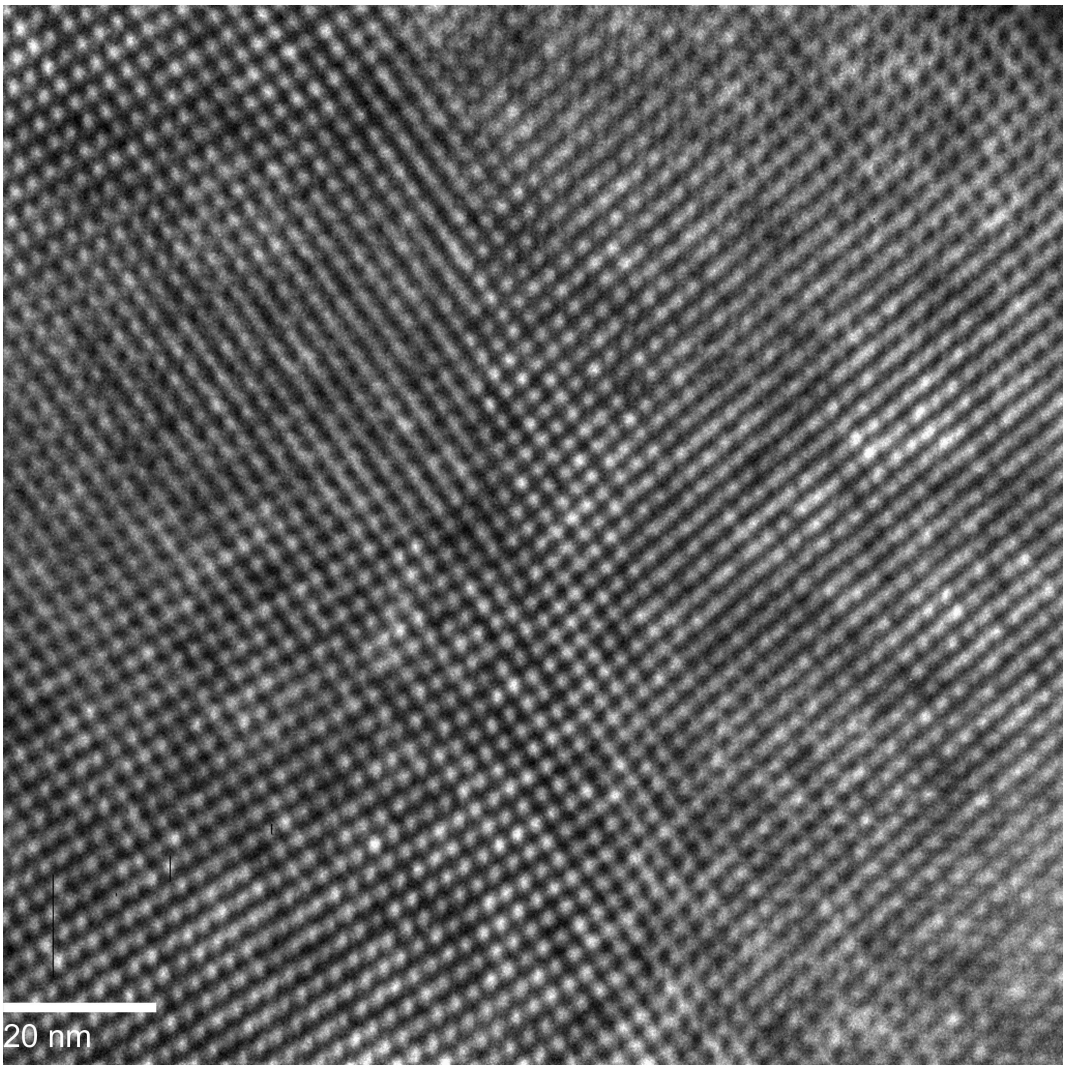

Figure 4.15: HREM image of a domain boundary not exhibiting the transition zone suggested by Jian and Wayman.

domains must in some way be compensated, and some sort of adjustment is therefore probable.

In figure 4.16 we present a closeup of part of the boundary from figure 4.15 and a model for the domain boundary. The boundary is roughly parallel to the $(20\bar{6})$ and (602) planes of the two domains. This orientation is somewhat different from that observed in SAD, but considering that the HREM image is a very local observation of the boundary, this is of no great concern.

4.2.3 Investigation of segregation to the domain boundary

It is well known that impurities often diffuse to grain boundaries and other imperfections in the lattice. If we consider atoms as hard spheres, this can be explained by the fact that these lattice imperfections often are disordered areas with a lot of “free” space where the impurity atoms can fit without straining the lattice.

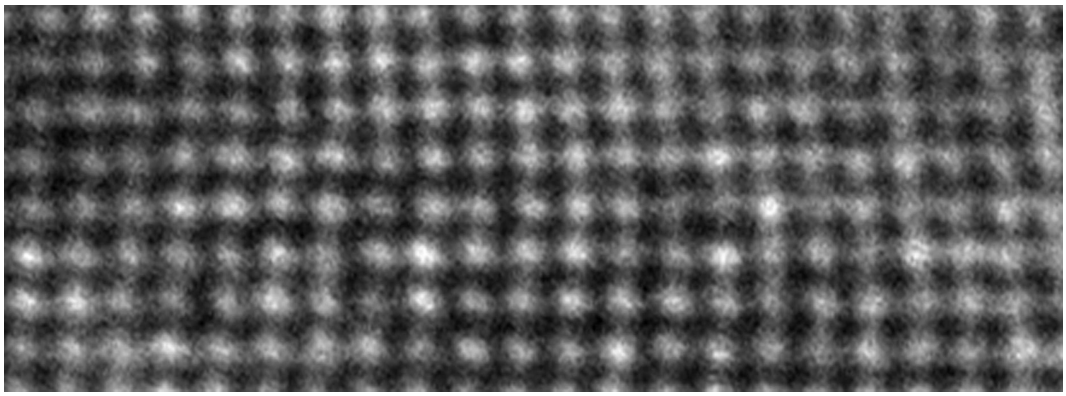

(a) Closeup of the domain boundary in figure 4.15.

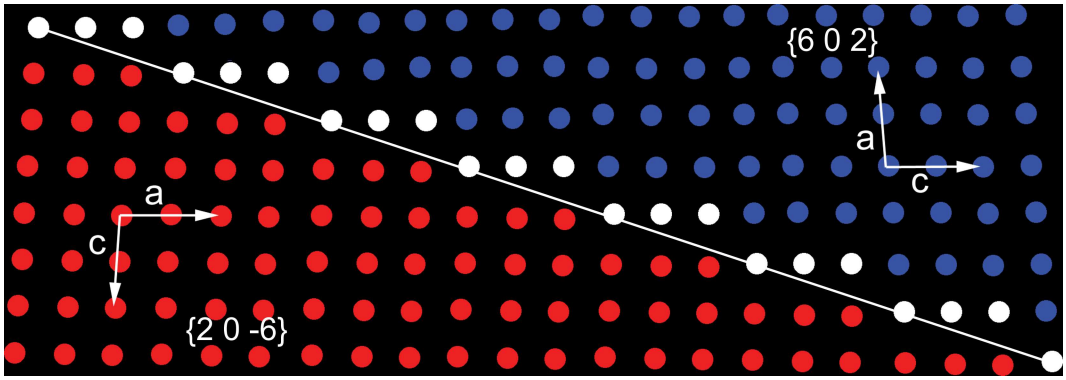

(b) Model of the domain boundary. The boundary is roughly parallel to the $(20\bar{6})$ and (602) planes of the two domains, the white dots mark the columns that are mutual to the two domains.

Figure 4.16: Direct observation of the domain boundary, and a schematic model of the lattice orientation on both sides of the boundary.

Thus the energy of the entire system is reduced by allowing a larger concentration of the impurity atoms near imperfections than elsewhere in the lattice.

In chapter 2.4.2 we found that the ideal length of the $Sr - O$ bond is longer than the ideal length of both the $La - O$ and $Nb - O$ bonds. As a first approximation we view the atoms as hard spheres. The strontium atoms may then be considered to have a larger diameter than both the lanthanum and niobium atoms. Introducing these larger spheres into the lattice will cause a strain and increased lattice energy. By extension of the argument in the previous paragraph, we might expect a higher concentration of Sr near the domain boundaries than in the interior of the domains.

Closer consideration of the domain boundary, however, leads us to expect little or no segregation of Sr to the boundary. Refering to figure 4.16 the reason for this is rather obvious. The domain boundary in question is highly ordered and allows for very little "free" space where the large Sr atoms could fit. Segregation of Sr to the domain boundary will therefore not reduce the strain energy of the lattice appreciably. Based on this model there is no reason to expect any noticable segragation of Sr to the domain boundary.

We must also consider how the specimen was synthesized. As mentioned earlier, the tetragonal to monoclinic phase transition takes place at approximately $500°C$. The domains structure appears only below this temperature, and any segregation towards the boundaries between domains would therefore have to occur at temperatures below $500°C$. At temperatures as low as this, the solid state diffusion rate is usually very low. Assuming that the sample was not held at $4 - 500°C$ for an extended amount of time, these considerations also lead us to expect no noticable segregation.

EDS analysis of the domain boundary confirms that there is little or no segregation of Sr to the boundary. Figure 4.17 shows a spectrum obtained along the boundary compared to a spectrum obtained a distance away from the boundary. The two spectra are virutally identical, indicating a homogeneous distribution of Sr.

The "hard-spheres" model is only a first approximation to the problem. A more in-depth analysis would entail considering the bonding-evironment at the boundary. It would not be unreasonable to imagine that the coordination of oxygen atoms with respect to the cation sites could be different at the interface than away from it. This in turn could make it more or less energetically favourable for the Sr to segregate to the boundary. Considerations of this kind are rather complicated, and we shall not discuss them further. Readers may refer to de Fontaine and Wille [20] for examinations of this kind for the $YBCO$ system.

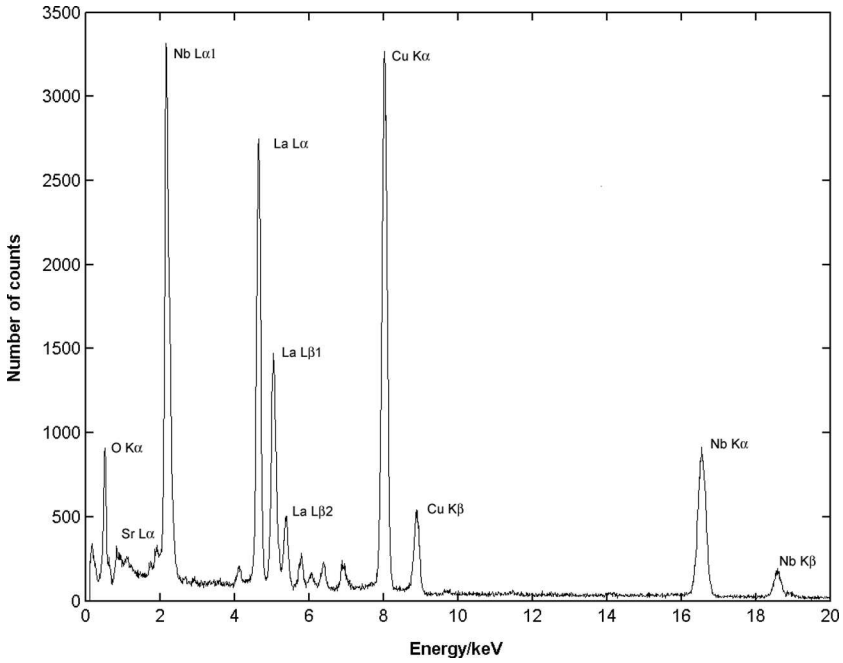

(a) EDS spectrum obtained at the boundary.

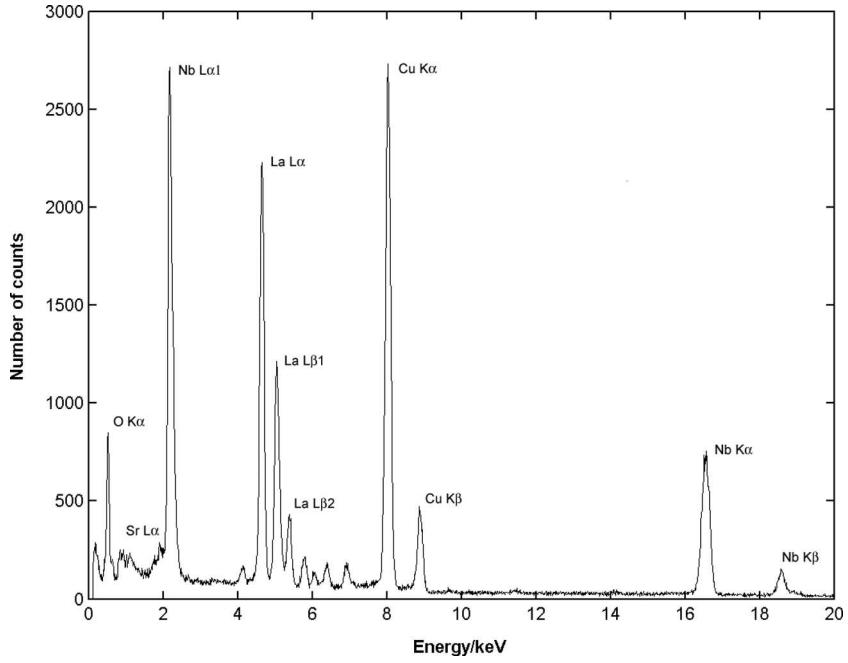

(b) EDS spectrum obtained away from the boundary.

Figure 4.17: EDS spectra obtained at the boundary and away from it. There is no indication of segregation of Sr either to or from the boundary.

Chapter 5

Discussion

5.1 The crystal structure of the Sr-rich phase

The crystal structure of the Sr-rich phase has been determined to be orthorhombic or monoclinic with cell parameters $a = 7.91$Å, $b = 5.81$Å and $c = 30.75$Å. A Sr:Nb ratio between 1:2 and 1:3 has been suggested.

A search in the Inorganic Crystal Structure Database (ICSD) reveals few reported structures that match these properties. The most promising are a $SrNb_2O_6$ phase reported by Marinder [21] and a reduced $Sr_2Nb_5O_9$ reported by Svensson [22]. These phases match the composition we have indicated earlier. Crystal structure data for these two phases are summarized in table 5.1 together with cell parameters from the present study. Full ICSD entries are included in appendix C, and the crystal structures are illustrated in figure 5.1.

A first glance at the dimensions of the unit cells suggest that the phase we have discovered differs greatly from the phase reported by Svensson [22]. Furthermore, we do not expect to find great similarities with the structure reported by Svensson, since this phase was intentionally kept low in oxygen, suggesting Nb^{3+} valence rather than Nb^{5+}.

The cell parameters of the phase reported by Marinder [21] shows similarity with the parameters found in the present study. It is possible that the Sr-rich phase we have studied is related to the phase reported by Marinder. This phase has composition and lattice parameters similar to the fluorite and perovskite structures.

Marinder has reported a unit cell with axes $a_M = 7.7223$ Å and $b_M = 5.5944$ Å. The ratio between these axes is approximately $\sqrt{2}$, suggesting that the a_M-axis may actually be a diagonal along one of the faces in a near-cubic structure with cell parameters close to b_M. This is illustrated in figure 5.2(a). A typical lattice parameter for many fluorite structures is $a_F = 5.5$ Å, which is close to b_M. The structure described by Marinder shows similarities to a fluorite structure with an alternative unit cell.

We may also consider this structure from the point of view of a perovskite cell. The cubic perovskite typically has $a_P = 4$Å $\approx \frac{1}{2}\sqrt{2} \cdot a_F$, that is, half the diagonal along the face of the fluorite structure. This is illustrated in figure 5.2(b). In this case, the diagonal d will have length $d = \sqrt{2} \cdot a_P = \frac{1}{2}\sqrt{2} \cdot \sqrt{2} \cdot a_F = a_F$, which we have seen is approximately equal to b_M.

Table 5.1: Crystallographic data for the phases reported by Svensson and Marinder and lattice parameters for the phase observed in the present study.

	Crystal structure	Space group	a/Å	b/Å	c/Å	β
Svensson [22]	Tetragonal	$P4/mmm$	4.1405	4.1405	12.040	90°
Marinder [21]	Monoclinic	$P2_1/c$	7.7223	5.5944	10.9862	90.372°
Present study	–	–	7.91	5.81	30.75	–

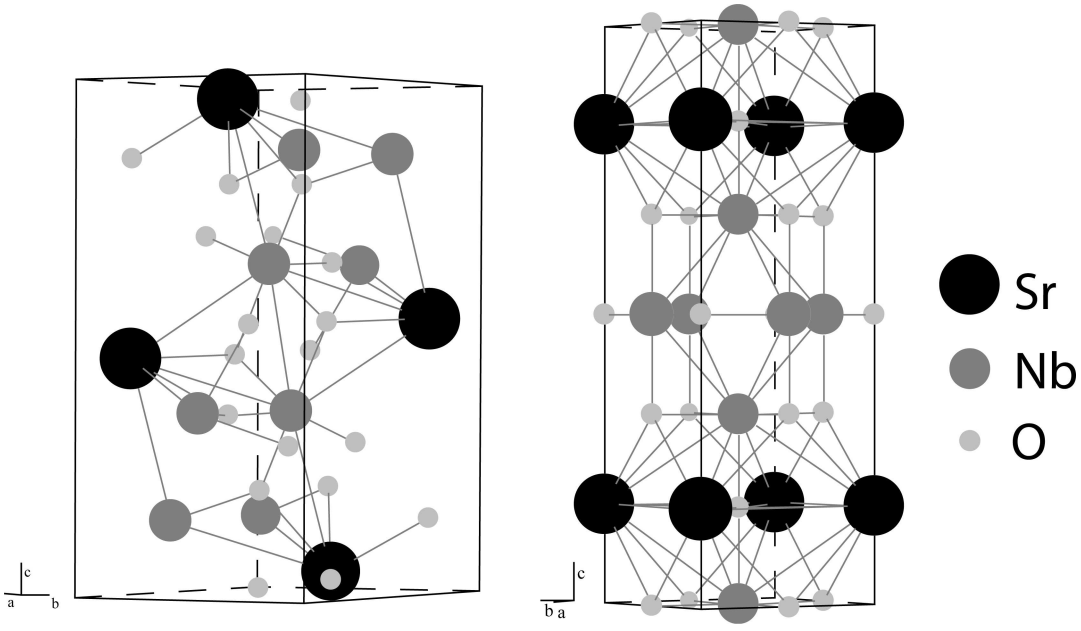

Figure 5.1: The crystal structures reported by Marinder (left) and Svensson (right).

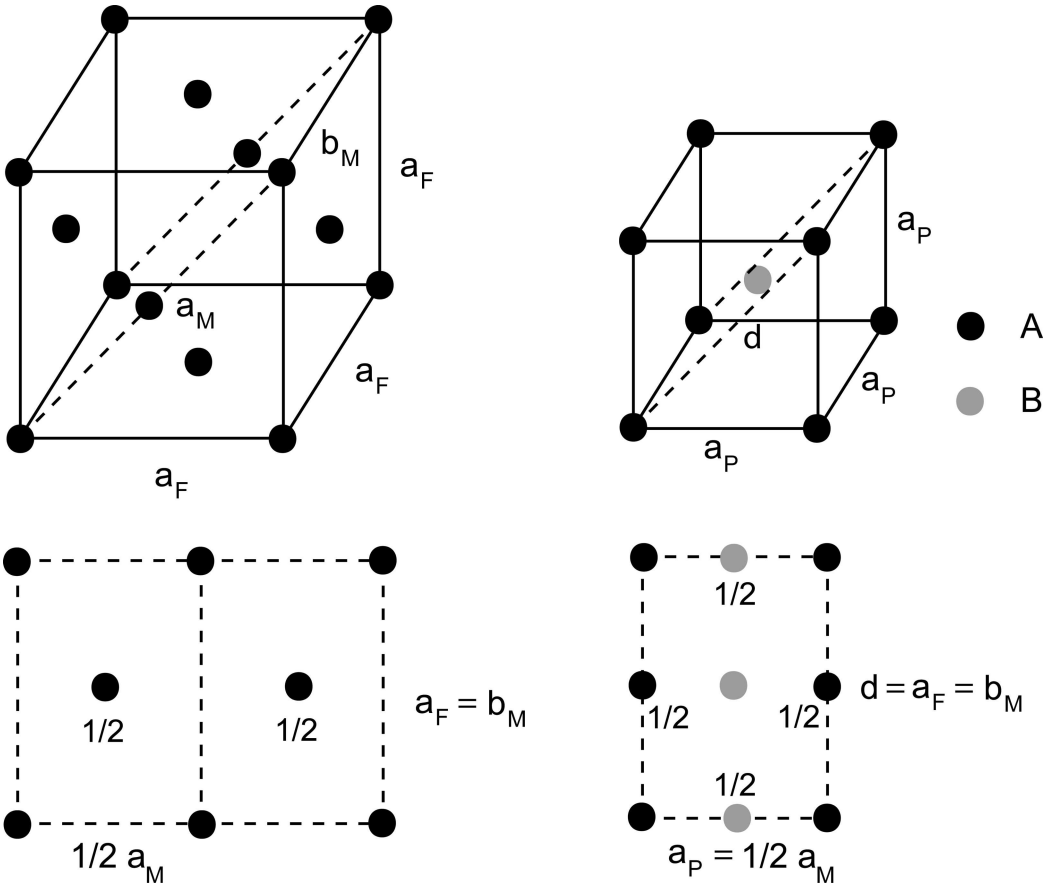

(a) A fluorite structure (top). The $\{110\}$ plane (dotted lines) is a possible orientation of the unit cell reported by Marinder. This plane is sketched at the bottom.

(b) A perovskite structure (top). The $\{110\}$ plane (dotted lines) is a possible orientation of the unit cell reported by Marinder. This plane is sketched at the bottom.

Figure 5.2: Illustrations of the possible relationship between the phase reported by Marinder and a fluorite and perovskite structure. Only cation sites are indicated.

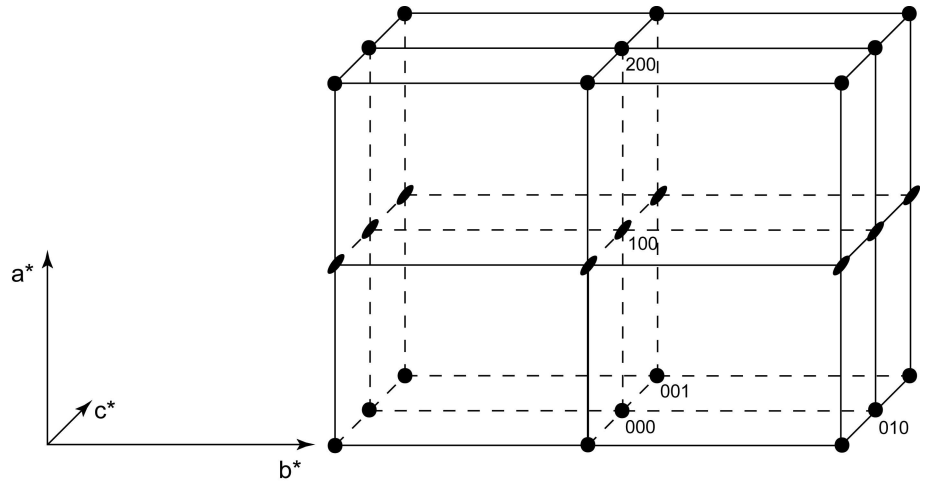

Figure 5.3: Sketch of the reciprocal lattice of the Sr-rich phase. Notice the elongation of reflections $hkl : h = 2n + 1$ in the $\mathbf{c}^*$ direction.

These considerations suggest a relationship between the structure reported by Marinder and a fluorite and/or perovskite structure. The Sr-rich phase in our studies may be a related to this structure, differing for example due to compositional differences.

We have observed diffuse scattering around reciprocal coordinates $hkl : h = 2n+1$. This diffuse scattering can be seen as elongated streaks along the c^* axis, this is illustrated in figure 5.3.

This diffuse scattering suggests a disorder in the stacking of domains along the c axis. The fact that diffuse scattering is observed for indices $hkl : h = 2n + 1$ indicates that the domains are shifted along the a axis with a magnitude of $a/2$. This is illustrated in figure 5.4 with domains of height $d = c$. In most cases the actual height of each domain will be much larger, consisting of a perfect stacking of unit cells over a long distance, before a shift along the a axis occurs. The height of the domains may be estimated by the size of the streaks in the diffraction patterns. A rough estimate suggests that the height of the domains in our case is in the order of 50 Å.

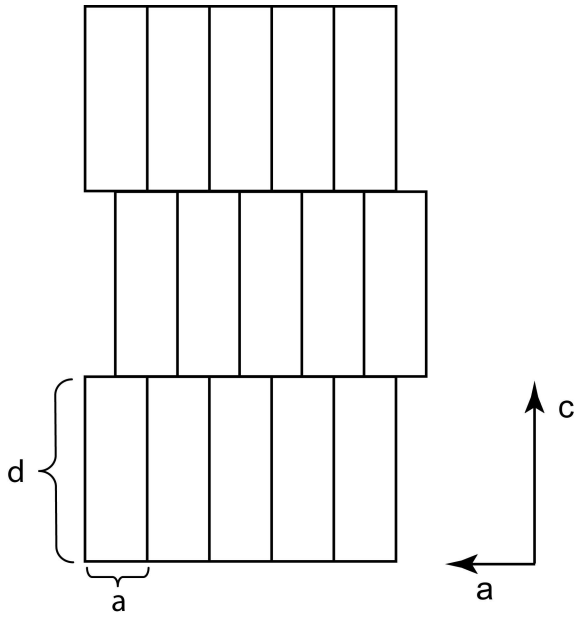

Figure 5.4: Sketch illustrating a possible stacking disorder causing the diffuse scattering observed.

5.2 The Domain structure of $LaNbO_4$

5.2.1 The orientation of domain boundaries

As seen in chapter 4.2.1, we have found the boundary between domains to be approximately parallel to the $(2\ 0\ \bar{5})_I/(5\ 0\ 2)_{II}$ planes of the two domains. Based on the diffraction pattern in figure 4.13(a) we can determine the exact orientation of the boundary.

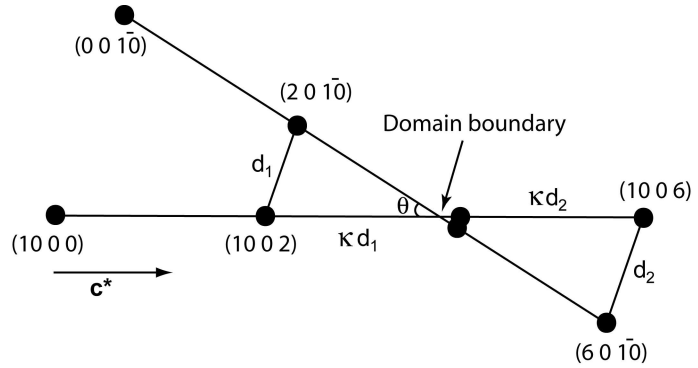

Figure 5.5: Sketch of the arrangement of diffraction spots. Notice that no spots are located at the intersect of the two lattices.

Figure 5.5 shows the arrangement of diffraction spots in the region of the spots corresponding to the $(4\ 0\ \overline{10})_I/(10\ 0\ 4)_{II}$ planes in the $[010]$ projection. To identify the exact index of the domain boundary, we must find the coordinates of the intersect between the two lines, indicated in figure 5.5. This intersect corresponds to the lattice planes that have the exact same orientation in the two domains. Notice

that no diffraction spots are located at the intersect, indicating that the domain boundary has a non-integer index.

The two triangles in figure 5.5 are geometrically similar, and their sides are therefore related by some constant of proportionality. We designate one such constant κ, and refer to the distance between the $(10\,0\,2)$ lattice site and the intersect as κd_1, and the distance between the intersect and the $(10\ 0\ 6)$ lattice site as κd_2, as indicated in the figure. The vector $\mathbf{c}^*$ is a unit vector of one of the reciprocal lattices with length c^*.

The intersect is located at some point with index $(10\ 0\ l)$, and studying figure 5.5 we find that the value of l may be found by use of the the following formula:

$$l = 2c^* + \frac{4c^*}{\kappa d_1 + \kappa d_2}\kappa d_1 \tag{5.1}$$

Exact measurements of d_1 and d_2 give us $l = 3.921875c^*$, and we conclude that the domain boundary is parallel to the $(3.921875\ 0\ \overline{10})_I/(10\ 0\ 3.921875)_{II}$ planes of the two domains. For easy comparison with the previous results, we may refer to the parallel planes $(2\ 0\ \overline{5.10})_I/(5.10\ 0\ 2)_{II}$.

We have previously seen that Jian and Wayman have predicted that the orientation of the boundary should be parallel to the $(2\ 0\ \overline{4.04})_I/(4.04\ 0\ 2)_{II}$ planes [7]. This prediction was done using the strain tensor formalism and results of Aizu [9] [8] and Sapriel [11]. It seems, however, that they have not been able to present direct observations confirming their predictions. Their calculations are also at odds with the experimental results and calculations of Tsunekawa and Takei [6], who have predicted a boundary parallel to the $(2\ 0\ \overline{5.07})_I/(5.07\ 0\ 2)_{II}$ planes, and observed a a boundary parallel to the $(2\ 0\ \overline{5.10})_I/(5.10\ 0\ 2)_{II}$ planes. As we have seen, our experimental results are in excellent agreement with both the predictions and result of Tsunekawa and Takei.

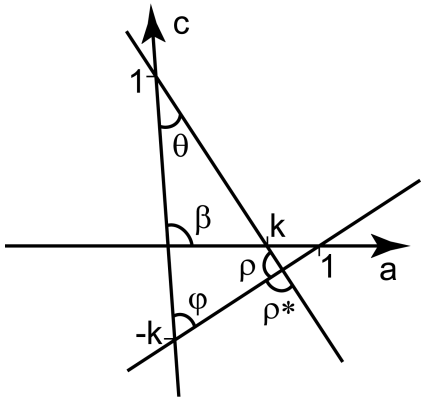

Figure 5.6: Illustration of the the orientational relationship between the boundary planes in the two domains.

Since ferroelastic theory seems unable to successfully predict the orientation of the domain boundaries, we develope an alternative method of predicting this orientation. We consider the strain comaptability criterion proposed by Sapriel (see appendix A.3). This criterion states that the domain wall is the plane in which lengths change an equal amount in both domains during the phase transition.

We wish to determine the value of m so that the boundary is parallel to the $(2\ 0\ \overline{m})_I/(m\ 0\ 2)_{II}$ planes. As these planes are parallel to the b axis, we view the system in the $[010]$ projection where the boundary planes

are represented by lines. Since the lengths of the lines representing the planes are equal in the tetragonal phase, we immediately realize that their lenghts must also be equal in the monoclinic phase if the strain compatability criterion is to be satisfied.

Figure 5.6 illustrates the orientation of the two planes $(1\ 0\ -\frac{1}{k})$ and $(\frac{1}{k}\ 0\ 1)$ viewed in the $[010]$ projection. Based on this figure, we can derive the explicit expression for "one unit" of length for the two planes. That is, the length of that part of the line representing the individual plane that falls between the a and c axes:

$$d_I^2 = a^2 + (kc)^2 - 2akc \cdot \cos(180^\circ - \beta) \tag{5.2}$$

$$d_{II}^2 = (ka)^2 + c^2 - 2kac \cdot \cos\beta \tag{5.3}$$

Requiring these lengths to be equal, i.e. $d_I^2 = d_{II}^2$, allows us to solve for the parameter k, which is the intersect of the plane with the a and c axes:

$$k = \frac{2ac \cdot \cos\beta \pm \sqrt{4a^2c^2\cos^2\beta - 2a^2c^2 + a^4 + c^4}}{(a^2 - c^2)} \tag{5.4}$$

Given that we know the cell parameters of the monoclinic phase, we can now calculate the value of m through the relation $m = \frac{2}{k}$. Table 5.2 compares some predicted values of m.

Table 5.2: Values of m predicted by Jian and Wayman, Tsunekawa and Takei and an alternative method using cell parameters from the present study and reported by Tsunekawa and Takei.

		a/Å	b/Å	c/Å	β	Orientation, m
Predictions made by:	Jian and Wayman [7]					4.04
	Tsunekawa and Takei [6]					5.07
Alternative method	Present study	5.55	11.62	5.21	94.3°	5.47
using parameters from:	Tsunekawa and Takei [6]	5.5735	11.5418	5.2159	94.07°	5.07

We note that given the same cell parameters, our alternative method predicts the same boundary orientation as the calculations done by Tsunekawa and Takei. This orientation is in excellent agreement with our observations of the boundary. There seems to be no evidence supporting the orientation suggested by Jian and Wayman.

It is also interesting to note that the predicted orientation of the boundary relies heavily on the cell parameters of the monoclinic phase, and that even small changes in cell parameters will cause quite noticable changes in orientation of the boundary. This is especially interesting in regard to the orientation of the boundary during the phase transition.

As noted in chapter 2.3, the tetragonal to monoclinic transition has been reported to be of the second order. Jian and Wayman have reported values for the cell parameters for several temperatures [14], and we see that the parameters change continually near the transition temperature, see table 5.3. Based on this we can expect the orientation of the domain boundaries to change during the transition from the tetragonal to the monoclinic phase.

Using the parameters provided by Jian and Wayman we can calculate the orientation of the domain boundary during the transformation, table 5.3 gives the predicted orientation for several temperatures.

Table 5.3: The orientation of the domain boundary predicted for several temperatures based on data provided by Jian and Wayman [14].

Temperature ($^\circ C$)	$a/$Å	$b/$Å	$c/$Å	β	Orientation, m
21	5.6330	11.6660	5.2610	94.1500	5.0290
300	5.5960	11.7450	5.3140	93.0100	4.8800
400	5.5650	11.7650	5.3560	92.2500	4.9152
470	5.5300	11.7780	5.3810	91.5300	4.7515
480	5.5250	11.7830	5.3950	91.2200	4.4711
490	5.5200	11.7940	5.3910	91.1500	4.3204
495	5.5020	11.7970	5.4050	91.0000	4.7641
500	5.4930	11.7890	5.4110	90.8600	4.8212
505	5.4940	11.7940	5.4250	90.7600	4.9981
510	5.4910	11.7990	5.4280	90.5100	4.0685
515	5.4820	11.7940	5.4350	90.3800	4.0650

These calculations suggest that the orientation of the domain boundary will vary with changing temperature, before ending up at approximately $(2\ 0\ \overline{4})/(4\ 0\ 2)$ in the tetragonal case. Unfortunately, there seems to be no experimental observation of the boundaries at different temperatures.

5.2.2 The orientational relationship between domains

The crystal structure of the two domains are related by a rotation about the $[010]$ axis. Our studies have found the rotational angle to be slightly more than 95°. Jian and Wayman have reported a rotation of 95.6° [7], while Tsunekawa and Takei imply that the rotational relationship is equal to β [6].

Studying figure 5.6, we can derive an expression for the orientational relationship between the domains. In order for the given boundary planes to be parallel, we see that the crystal structure must be related through a rotation of ρ or ρ^* about the b-axis. We have:

$$\rho = 180^\circ - \theta - \varphi \tag{5.5}$$

We have already argued that $d_I = d_{II} = d$, and using the law of sines we may now determine θ and φ:

$$\frac{d}{\sin\beta} = \frac{ka}{\sin\theta} \Rightarrow \sin\theta = \frac{ka\cdot\sin\beta}{d} = \frac{ka\cdot\sin\beta}{\sqrt{(ka)^2 + c^2 - 2kac\cdot\cos\beta}} \tag{5.6}$$

Here we have substituted the expression (5.3) into the above equation. The same procedure also yields:

$$\sin\varphi = \frac{a\cdot\sin(180^\circ - \beta)}{\sqrt{(ka)^2 + c^2 - 2kac\cdot\cos\beta}} \tag{5.7}$$

An explicit calculation using the call parametrs provided by Tsunekawa et al. [15] at room temperature,

Table 5.4: The orientational relationship ρ and ρ^* between domains as a function of temperature, compared to the monoclinic angle, β. The calculations are based on cell parameters provided by Jian and Wayman [14].

Temperature ($^\circ C$)	β(deg)	ρ(deg)	ρ^*(deg)
21	94.15	84.30	95.70
300	93.01	85.78	94.22
400	92.25	86.86	93.14
470	91.53	87.81	92.19
480	91.22	88.17	91.83
490	91.15	88.22	91.78
495	91.00	88.57	91.43
500	90.86	88.78	91.22
505	90.76	88.95	91.05
510	90.51	89.17	90.84
515	90.38	89.38	90.62

yields a rotational relationship between the two domains of $\rho = 84.37$ and $\rho^* = 95.63$. The latter value is larger than β by approximately 1.5°, which is slightly more than we have found experimentally. This result is, however, in good agreement with the findings of Jian and Wayman.

Since the magnitude of this rotation depends on the cell parameters, we investigate how the relationship between the domains varies with changing temperature. Table 5.4 lists values of ρ and ρ^* compared to β calculated for the cell parameters provided by Jian and Wayman [14] for different temperatures.

Our calculations predict values of ρ^* that are systematically different from the monoclinic angle β, and from the equations (5.5), (5.6) and (5.7) there seems to be no reason to expect a direct correspondence between the rotational relationship between the domains and β.

Chapter 6

Conclusions and recommendations

6.1 Main conclusions

Based on our studies we draw the following conclusions:

- The attempt to acheive 5% Sr doping of $LaNbO_4$ has failed. The sample has separated into two distinct phases.
- We have identified one of the phases as $LaNbO_4$ with a Sr doping of less than 3%.
- The Sr doping has not distorted the crystal structure or lattice parameters noticably.
- Our studies have revealed no segregation of Sr to the domain boundaries.
- We have experimentally detetermined that the domain boundary in $LaNbO_4$ is oriented parallel to the $(2\ 0\ \overline{5.10}/(5.10\ 0\ 2)$ planes of the two domains. This result is in excellent agreement with our calculations predicting an orientation of $(2\ 0\ \overline{5.07}/(5.07\ 0\ 2)$ at room-temperature.
- The theory of ferroelasticity as implemented by Jian and Wayman seems unable to successfully predict the orientation of domain boundaries in $LaNbO_4$.
- We have presented evidence supporting a sharp transition between two domains, as opposed to the diffuse transition suggested by Jian and Wayman.
- We have presented calculations predicting the orientational relationship between the crystal structure of adjacent domains. These calculations are in good agreement with our observations using SAD, and in excellent agreement with the experimental results of other workers.
- The Sr-rich phase has been identified as a strontium niobate with a Sr:Nb ratio between 1:3 and 1:2. The crystal structure has been determined to be orthorhombic or monoclinic with lattice parameters $a = 7.91$Å, $b = 5.81$Å and $c = 30.75$Å. The diffuse scattering observed is evidence of a stacking disorder along the $\mathbf{c}^*$ axis of the Sr-rich phase.

6.2 Suggestions for future work

- In situ studies of the rotation of domain boundaries in $LaNbO_4$ with temperature should be performed to test the validity of our predictions regarding the orientation of the domain boundaries.
- Further effort should be done to reveal the crystal structure and stacking disorder in the Sr-rich phase using convergent beam electron diffraction, high resolution electron microscopy and energy dispersive X-ray spectroscopy. To complement these techniques, X-ray diffractions studies should be performed assuming that samples with a higher fraction of the Sr-rich phase can be synthesized.

Appendix A

Some mathematical derivations

A.1 Rotation of transformation matrices

This derivation is in essence the same as that given by Khachaturyan [10].

Let the set of vectors $\{\mathbf{r}_1^p\}$ describe the lattice points of a crystal. We call this the *parent phase* (hence the superscript). We assume that this lattice belongs to a point group containing n operations of symmetry, with the corresponding matrix representations $\{\hat{\mathbf{G}}_1, \ldots, \hat{\mathbf{G}}_n\}$.

Let one of these matrices transform the initial vector $\mathbf{r}_1^p$:

$$\mathbf{r}_i^p = \hat{\mathbf{G}}_i \mathbf{r}_1^p$$

The set of vectors $\{\mathbf{r}_i^p\}$ coincide with those of $\{\mathbf{r}_1^p\}$ since $\hat{\mathbf{G}}_i$ is an operation of symmetry for the parent phase.

Operations of symmetry do not change the length of vectors, only their orientation. Operators of this kind, and their matrix representations, are called *unitary* and have the following properties:

$$\hat{\mathbf{G}}_i^\dagger = \hat{\mathbf{G}}_i^{-1} \Leftrightarrow \hat{\mathbf{G}}_i^\dagger \hat{\mathbf{G}}_i = \hat{\mathbf{I}} \tag{A.1}$$

Here $\hat{\mathbf{I}}$ is an $n \times n$ matrix such that $\hat{\mathbf{M}}\hat{\mathbf{I}} = \hat{\mathbf{M}}$ where $\hat{\mathbf{M}}$ is an arbitrary $n \times n$ matrix.

$\hat{\mathbf{G}}_i^\dagger$ is the transposed conjugate of the the matrix $\hat{\mathbf{G}}_i$.

Let $\hat{\mathbf{A}}_1$ be the matrix representation of a transformation causing a rearrangement of the lattice points so that:

$$\mathbf{r}_1^t = \hat{\mathbf{A}}_1 \mathbf{r}_1^p \tag{A.2}$$

The transformed lattice is now described by the set of points $\{\mathbf{r}_1^t\}$. We apply one of the operations of symmetry on both sides of equation A.2:

$$\hat{\mathbf{G}}_i\mathbf{r}_1^t = \hat{\mathbf{G}}_i\hat{\mathbf{A}}_1\mathbf{r}_1^p$$

We substitute $\hat{\mathbf{G}}_i\mathbf{r}_1^t = \mathbf{r}_i^t$ into the left side of this expression and use the properties (A.1):

$$\mathbf{r}_i^t = \hat{\mathbf{G}}_i\hat{\mathbf{A}}_1\hat{\mathbf{I}}\mathbf{r}_1^p = \hat{\mathbf{G}}_i\hat{\mathbf{A}}_1(\hat{\mathbf{G}}_i^\dagger\hat{\mathbf{G}}_i)\mathbf{r}_1^p = \hat{\mathbf{G}}_i\hat{\mathbf{A}}_1\hat{\mathbf{G}}_i^\dagger(\hat{\mathbf{G}}_i\mathbf{r}_1^p) = \hat{\mathbf{A}}_i\mathbf{r}_i^p$$

with $\hat{\mathbf{A}}_i = \hat{\mathbf{G}}_i\hat{\mathbf{A}}_1\hat{\mathbf{G}}_i^\dagger$.

The set of lattice points $\{\mathbf{r}_i^p\}$ coincides with $\{\mathbf{r}_1^p\}$ since $\hat{\mathbf{G}}_i$ is an operation of symmetry for the parent phase. The two sets $\{\mathbf{r}_i^t\}$ and $\{\mathbf{r}_1^t\}$, however, do not coincide since $\hat{\mathbf{G}}_i$ does not represent an operation of symmetry for the transformed phase [1].

Since the unitary operators do not change the length of vectors, $\{\mathbf{r}_1^t\}$ and $\{\mathbf{r}_i^t\}$ correspond to the same lattice, but differ with respect to orientation. In other words: both the matrix

$$\hat{\mathbf{A}}_i = \hat{\mathbf{G}}_i\hat{\mathbf{A}}_1\hat{\mathbf{G}}_i^\dagger$$

and $\hat{\mathbf{A}}_1$ describe the rearrangement of crystal lattice points that take place in the transformation, the two differing only in orientation.

A.2 Calcualtion of strain tensor components

Schlenker et al. [12] have given us the general expressions for strain tensor components before and after a transformation expressed by the crystal lattice parameters before and after thetransformation:

$$\begin{aligned}
l_{11} &= \frac{a_1 \sin\beta_1 \sin\gamma_1^*}{a_0 \sin\beta_0 \sin\gamma_0^*} - 1 \\
l_{22} &= \frac{b_1 \sin\alpha_1}{b_0 \sin\alpha_0} - 1 \\
l_{33} &= \frac{c_1}{c_0} - 1 \\
l_{12} = l_{21} &= \frac{1}{2}\left[\frac{b_1 \sin\alpha_1 \cos\gamma_0^*}{b_0 \sin\alpha_0 \sin\gamma_0^*} - \frac{a_1 \sin\beta_1 \cos\gamma_1^*}{a_0 sin\beta_0 \sin\gamma_0^*}\right] \\
l_{13} = l_{31} &= \frac{1}{2}\left[\frac{a_1 \cos\beta_1}{a_0 \sin\beta_0 \sin\beta_0^*} + \frac{\cos\gamma_0^*}{\sin\gamma_0^*} \times \left(\frac{b_1 \cos\alpha_1}{b_0 \sin\alpha_0} - \frac{c_1 \cos\alpha_0}{c_0 \sin\alpha_0}\right) - \frac{c_1 \cos\beta_0}{c_0 \sin\beta_0 \sin\gamma_0^*}\right] \\
l_{23} = l_{32} &= \frac{1}{2}\left[\frac{b_1 \cos\alpha_1}{b_0 \sin\alpha_0} - \frac{c_1 \cos\alpha_0}{c_0 \sin\alpha_0}\right]
\end{aligned}$$

[1] This is the general case. There are, of course, many cases where a particular operation of symmetry is retained during a transformation.

Here the lattice parameters before the transformation are: $\{a_0, b_0, c_0, \alpha_0, \beta_0, \gamma_0\}$ and the parameters after are $\{a_1, b_1, c_1, \alpha_1, \beta_1, \gamma_1\}$[2].

We label the parameters with the subscripts T for the tetragonal (initial) phase, and M for the monoclinic (final) phase. Remembering that the c_T axis corresponds to the b_M axis, we rename the parameters of the above equations and take into account the specific angles between the axes:

$$\begin{aligned} a_0 = b_0 &= a_T \\ c_0 &= c_T \\ a_1 &= c_M \\ b_1 &= a_M \\ c_1 &= b_M \\ \alpha_0 = \beta_0 = \gamma_0 = \alpha_T = \beta_T = \gamma_T &= 90^\circ \\ \alpha_1 = \beta_1 = \alpha_M = \gamma_M &= 90^\circ \\ \gamma_1 = \beta_M &\neq 90^\circ \end{aligned}$$

With this in mind, we arrive at the final results for the strain tensor components:

$$\begin{aligned} l_{11} &= \frac{c_M \sin\beta_M^*}{a_T} - 1 \\ l_{22} &= \frac{a_M}{a_T} - 1 \\ l_{33} &= \frac{b_M}{c_T} - 1 \\ l_{12} &= -\frac{1}{2}\frac{c_M \cos\beta_M^*}{a_T} \\ l_{21} &= l_{12} \\ \{l_{13}, l_{31}, l_{23}, l_{32}\} &= 0 \end{aligned}$$

A.3 The strain compatability criterion

Sapriel states that the permissible domain walls "*must contain all directions for which the change in length of any infinitesimal vector of the prototype, take the same value in the two adjacent domains*" [11]. This seems a reasonable criterion as it must be equally valid to view the plane in which the domain boundary lies as beloning to either one of the domains. The plane can not experience one level of deformation when viewed as belonging to one domain, and another level of deformation when belonging to the other domain.

In order to derive a mathematical expression for this criterion, let us consider a system where two points are connected by a very small vector $\mathrm{d}\vec{l}$. The length of this vector is $\mathrm{d}l = \sqrt{\mathrm{d}x_1^2 + \mathrm{d}x_2^2 + \mathrm{d}x_3^2}$ or $\mathrm{d}l^2 = \mathrm{d}x_i^2$. We now let the system deform somewhat so that the same two pints now are conneted by the vector $\mathrm{d}\vec{l'}$ with the lenght

[2] Si noe om at γ^* er komplementærvinkelen

$$\mathrm{d}l'^2 = \mathrm{d}x_1'^2 + \mathrm{d}x_2'^2 + \mathrm{d}x_3'^2 = \mathrm{d}x_i'^2 = (\mathrm{d}x_i + \mathrm{d}u_i)^2 \tag{A.3}$$

Here $\mathrm{d}u_i$ is the small displacement caused by the deformation: $\mathrm{d}u_i = (\frac{\partial u_i}{\partial x_k})\mathrm{d}x_k$, and u_i are the components of the displacement vector. We now have:

$$\mathrm{d}l'^2 = (\mathrm{d}x_i + \mathrm{d}u_i)^2 = \mathrm{d}l^2 + 2\mathrm{d}u_i\mathrm{d}x_i + \mathrm{d}u_i^2 = \mathrm{d}l^2 + 2\frac{\partial u_i}{\partial x_k}\mathrm{d}x_k\mathrm{d}x_i + \frac{\partial u_i}{\partial x_k}\frac{\partial u_i}{\partial x_l}\mathrm{d}x_k\mathrm{d}x_l$$

We recall that summation is implied with respect to subscripts appearing twice in an expression. Interchanging subscripts is equivalent to changing the order of summation, and since summation is commutative, does not affect the result.

The above expression can now be rewritten:

$$\mathrm{d}l'^2 = \mathrm{d}l^2 + 2\frac{\partial u_k}{\partial x_i}\mathrm{d}x_k\mathrm{d}x_i + \frac{\partial u_l}{\partial x_k}\frac{\partial u_l}{\partial x_i}\mathrm{d}x_k\mathrm{d}x_i = \mathrm{d}l^2 + 2u_{ik}\mathrm{d}x_i\mathrm{d}x_k \tag{A.4}$$

Here u_{ik} is the strain tensor defined as:

$$u_{ik} = \frac{1}{2}\left(\frac{\partial u_i}{\partial x_k} + \frac{\partial u_k}{\partial x_i} + \frac{\partial u_l}{\partial x_i}\frac{\partial u_l}{\partial x_k}\right)$$

The expression (A.4) gives us the square lenght of the vector connecting two points after the deformation. The *change* in length can be obtained simply by subtracting the square of the length before deformation, $\mathrm{d}l^2$.

We now recall that our requirement for the plane of the domain wall is that a vector in this plane during transformation should change an equal amount in the two adjacent domains. The expression (A.4) is valid for one domain with the strain tensor u_{ik}, the equivalent expression for an adjacent domain with strain tensor u_{ik}^* is:

$$\mathrm{d}l'^{*2} = \mathrm{d}l^2 + 2u_{ik}^*\mathrm{d}x_i\mathrm{d}x_k \tag{A.5}$$

We now demand that the change in length be equal for the two domains:

$$2u_{ik}^*\mathrm{d}x_i\mathrm{d}x_k - 2u_{ik}\mathrm{d}x_i\mathrm{d}x_k \equiv 0$$

which is equvalent to the formulation presented by Sapriel.

Appendix B

Crystallographic data for $LaNbO_4$

We provide relevant crystallographic data from various sources for easy reference.

B.1 The high-temperature Scheelite structure

```
*data for   ICSD #37139
Coll Code   37139
Rec  Date   1983/12/31
Chem Name   Lanthanum Tetraoxoniobate
Structured  La Nb O4
Sum         La1 Nb1 O4
ANX         ABX4
D(calc)     5.77
Title       The High-Temperature Paraelastic Structure of La Nb O4
Author(s)   David, W.I.F.
Reference   Materials Research Bulletin
            (1983), 18, 749-756
Unit Cell   5.4009(2) 5.4009(2) 11.6741(2) 90. 90. 90.
Vol         340.53
Z           4
Space Group I 41/a S
SG Number   88
Cryst Sys   tetragonal
Pearson     tI24
Wyckoff     f b a
R Value     0.105
Red Cell    I  5.400 5.400 6.975 112.776 112.776 89.999 170.265
Trans Red   1.000 0.000 0.000 / 0.000 -1.000 0.000 / -0.500 0.500 -0.500
Comments    Temperature in Kelvin: 803
            At least one temperature factor is implausible or
            meaningless but agrees with the value given in the paper.
Atom  #   OX   SITE      x           y           z           SOF      H
 La   1  +3    4 b   0           0           0.5           1.         0
```

```
 Nb   1  +5    4 a   0           0           0              1.         0
 O    1  -2    16 f  0.2443(4)   0.1595(2)   0.0851(2)      1.         0
Lbl  Type      B11         B22         B33         B12         B13         B23
La1  La3+ 1.86(6)     1.86(6)     0.23(2)     0           0           0
Nb1  Nb5+ 1.27(7)     1.27(7)     0.47(2)     0           0           0
O1   O2-  2.32(6)     2.24(6)     0.46(1)     -.60(15)    -.18(3)     0.14(3)
*end for    ICSD #37139
```

B.2 The low-temperature Fergusonite structure

```
*data for   ICSD #73390
Coll Code   73390
Rec  Date   1994/06/30
Mod  Date   1997/05/13
Chem Name   Lanthanum Niobate
Structured  La (Nb O4)
Sum         La1 Nb1 O4
ANX         ABX4
D(calc)     5.91
Title       Precise structure analysis by neutron diffraction for R Nb O4 and
            distortion of Nb O4 tetrahedra
Author(s)   Tsunekawa, S.;Kamiyama, T.;Sasaki, K.;Asano, H.;Fukuda, T.
Reference   Acta Crystallographica A (39,1983-)
            (1993), 49, 595-600
Unit Cell   5.5647(1) 11.5194(2) 5.2015(1) 90. 94.100(1) 90.
Vol         332.57
Z           4
Space Group I 1 2/c 1
SG Number   15
Cryst Sys   monoclinic
Pearson     mI24
Wyckoff     f2 e2
R Value     0.016
Red Cell    I  5.201 5.564 6.829 112.343 110.589 94.1 166.287
Trans Red   0.000 0.000 -1.000 / -1.000 0.000 0.000 / 0.500 0.500 0.500
Comments    Neutron diffraction (powder)
            Rietveld profile refinement applied
            At least one temperature factor is implausible or
            meaningless but agrees with the value given in the paper.
Atom  #   OX   SITE      x           y           z           SOF      H
 La   1  +3    4 e   0           0.6292(1)   0.25           1.         0
 Nb   1  +5    4 e   0           0.1036(1)   0.25           1.         0
 O    1  -2    8 f   0.2376(2)   0.0337(1)   0.0546(2)      1.         0
 O    2  -2    8 f   0.1460(2)   0.2042(1)   0.4888(2)      1.         0
Lbl  Type      U11         U22         U33         U12         U13         U23
La1  La3+ 0.0052(5)   0.0007(5)   0.0058(5)   0           0.0028(4)   0
Nb1  Nb5+ 0.0018(6)   0.0024(6)   0.0049(7)   0           0.0005(5)   0
O1   O2-  0.0080(6)   0.0042(5)   0.0109(7)   0.0007(5)   0.0059(5)   0.0011(5)
O2   O2-  0.0063(6)   0.0043(5)   0.0066(6)   0.0005(5)   -.0008(4)   -
.0024(5)
*end for    ICSD #73390
```

B.3 D-values for the low-temperature Fergusonite

The d-values were calculated using the 'dvalue' program by Per Skjerpe, and the data from the previous section.

```
 LaNbO4 - Fergusonite. ICSD data #73390

0   A=  5.565       B= 11.519       C=  5.201
 ALFA= 90.000    BETA= 94.100   GAMMA= 90.000
0-------------------------------------------------

 LOWER LIMIT OF D-VALUES = 1.60 ANGSTROM

 VOLUME OF UNIT CELL =    332.57 CUBI*    ANGSTROM

 MAXIMUM VALUES OF H,K,L CONSIDERED:    4    8    4

 NUMBER OF REFLEXES FOUND:    50

-------------------------------------------------
0REFLECTIONS TREATED AS EQUIVALENT:
 -------------------------------------------------
              H  K  L
              H -K  L
             -H -K -L
             -H  K -L
 -------------------------------------------------
   NPERM= 4        XSYSTEM = 2        CENTRE= 5
 -------------------------------------------------
1 LaNbO4

0   A=  5.565       B= 11.519       C=  5.201
 ALFA= 90.000    BETA= 94.100   GAMMA= 90.000
0-------------------------------------------------------------------------
-------
0   H   K   L      D           H   K   L      D           H   K   L      D
0-------------------------------------------------------------------------
-------
    0   2   0     5.7597
    1   1   0     5.0003
    0   1   1     4.7305
    1   0  -1     3.9331
    1   0   1     3.6618
    1   2  -1     3.2480
    1   3   0     3.1578
    1   2   1     3.0902
    0   3   1     3.0864
    0   4   0     2.8798
    2   0   0     2.7752
    0   0   2     2.5941
    2   2   0     2.5001
    2   1  -1     2.4649
```

```
    1   1  -2     2.3658
    0   2   2     2.3653
    2   1   1     2.3284
    1   4  -1     2.3236
    1   4   1     2.2637
    1   1   2     2.2443
    1   5   0     2.1279
    2   3  -1     2.1087
    0   5   1     2.1056
    1   3  -2     2.0457
    2   3   1     2.0214
    2   4   0     1.9983
    2   0  -2     1.9665
    1   3   2     1.9656
    0   4   2     1.9274
    0   6   0     1.9199
    2   2  -2     1.8611
    2   0   2     1.8309
    3   1   0     1.8267
    3   0  -1     1.7835
    2   2   2     1.7449
    1   6  -1     1.7253
    0   1   3     1.7102
    3   0   1     1.7045
    3   2  -1     1.7037
    2   5  -1     1.7014
    1   6   1     1.7004
    1   0  -3     1.6857
    1   5  -2     1.6678
    3   3   0     1.6668
    2   5   1     1.6545
    3   2   1     1.6345
    2   4  -2     1.6240
    1   5   2     1.6235
    1   0   3     1.6186
    1   2  -3     1.6178
0-------------------------------------------------------------------------
-------
```

B.4 Spacegroup 15, C2/c

We present an excerpt of the International Tables of Crystallography [23] relevant to the low temperature phase of $LaNbO_4$.

$C\,2/c$ C_{2h}^6 $2/m$ Monoclinic

No. 15 $C\,1\,2/c\,1$ Patterson symmetry $C\,1\,2/m\,1$

UNIQUE AXIS b, CELL CHOICE 1

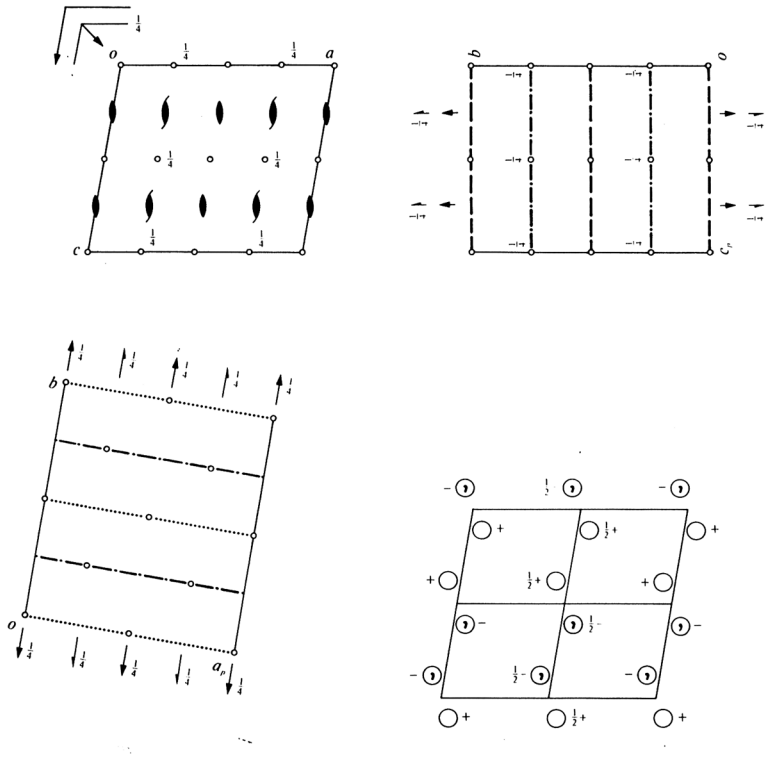

Origin at $\bar{1}$ on glide plane c

Asymmetric unit $0\leq x\leq\frac{1}{2};\quad 0\leq y\leq\frac{1}{2};\quad 0\leq z\leq\frac{1}{2}$

Symmetry operations

For (0,0,0)+ set

(1) 1 (2) 2 $0,y,\frac{1}{4}$ (3) $\bar{1}$ 0,0,0 (4) c $x,0,z$

For $(\frac{1}{2},\frac{1}{2},0)$+ set

(1) $t(\frac{1}{2},\frac{1}{2},0)$ (2) $2(0,\frac{1}{4},0)$ $\frac{1}{4},y,\frac{1}{4}$ (3) $\bar{1}$ $\frac{1}{4},\frac{1}{4},0$ (4) $n(\frac{1}{2},0,\frac{1}{2})$ $x,\frac{1}{4},z$

CONTINUED **No. 15** ***C* 2/*c***

Generators selected (1); $t(1,0,0)$; $t(0,1,0)$; $t(0,0,1)$; $t(\frac{1}{2},\frac{1}{2},0)$; (2); (3)

Positions

Multiplicity, Wyckoff letter, Site symmetry			Coordinates				Reflection conditions
			(0,0,0)+	$(\frac{1}{2},\frac{1}{2},0)+$			General:
8	*f*	1	(1) x,y,z	(2) $\bar{x},y,\bar{z}+\frac{1}{2}$	(3) $\bar{x},\bar{y},\bar{z}$	(4) $x,\bar{y},z+\frac{1}{2}$	hkl : $h+k=2n$ $h0l$: $h,l=2n$ $0kl$: $k=2n$ $hk0$: $h+k=2n$ $0k0$: $k=2n$ $h00$: $h=2n$ $00l$: $l=2n$
							Special: as above, plus
4	*e*	2	$0,y,\frac{1}{4}$	$0,\bar{y},\frac{3}{4}$			no extra conditions
4	*d*	$\bar{1}$	$\frac{1}{4},\frac{1}{4},\frac{1}{2}$	$\frac{3}{4},\frac{1}{4},0$			hkl : $k+l=2n$
4	*c*	$\bar{1}$	$\frac{1}{4},\frac{1}{4},0$	$\frac{3}{4},\frac{1}{4},\frac{1}{2}$			hkl : $k+l=2n$
4	*b*	$\bar{1}$	$0,\frac{1}{2},0$	$0,\frac{1}{2},\frac{1}{2}$			hkl : $l=2n$
4	*a*	$\bar{1}$	0,0,0	$0,0,\frac{1}{2}$			hkl : $l=2n$

Symmetry of special projections

Along [001] *c* 2*m m*
$\boldsymbol{a}'=\boldsymbol{a}_p$ $\boldsymbol{b}'=\boldsymbol{b}$
Origin at 0,0,*z*

Along [100] *p* 2*g m*
$\boldsymbol{a}'=\frac{1}{2}\boldsymbol{b}$ $\boldsymbol{b}'=\boldsymbol{c}_p$
Origin at *x*,0,0

Along [010] *p* 2
$\boldsymbol{a}'=\frac{1}{2}\boldsymbol{c}$ $\boldsymbol{b}'=\frac{1}{2}\boldsymbol{a}$
Origin at 0,*y*,0

Maximal non-isomorphic subgroups

I [2]*C* 1 2 1 (*C* 2) (1; 2)+
[2]*C* $\bar{1}$ (*P* $\bar{1}$) (1; 3)+
[2]*C* 1*c* 1 (*C c*) (1; 4)+

IIa [2]*P* 1 2/*c* 1 (*P* 2/*c*) 1; 2; 3; 4
[2]*P* 1 2/*n* 1 (*P* 2/*c*) 1; 2; (3; 4)+($\frac{1}{2},\frac{1}{2}$,0)
[2]*P* 1 2_1/*n* 1 (*P* 2_1/*c*) 1; 3; (2; 4)+($\frac{1}{2},\frac{1}{2}$,0)
[2]*P* 1 2_1/*c* 1 (*P* 2_1/*c*) 1; 4; (2; 3)+($\frac{1}{2},\frac{1}{2}$,0)

IIb none

Maximal isomorphic subgroups of lowest index

IIc [3]*C* 1 2/*c* 1 ($\boldsymbol{b}'=3\boldsymbol{b}$)(*C* 2/*c*); [3]*C* 1 2/*c* 1 ($\boldsymbol{c}'=3\boldsymbol{c}$)(*C* 2/*c*);
[3]*C* 1 2/*c* 1 ($\boldsymbol{a}'=3\boldsymbol{a}$ or $\boldsymbol{a}'=3\boldsymbol{a},\boldsymbol{c}'=-\boldsymbol{a}+\boldsymbol{c}$ or $\boldsymbol{a}'=3\boldsymbol{a},\boldsymbol{c}'=\boldsymbol{a}+\boldsymbol{c}$)(*C* 2/*c*)

Minimal non-isomorphic supergroups

I [2]*C m c m*; [2]*C m c a*; [2]*C c c m*; [2]*C c c a*; [2]*F d d d*; [2]*I b a m*; [2]*I b c a*; [2]*I m m a*; [2]*I* 4_1/*a*; [3]*P* $\bar{3}$ 1 2/*c*;
[3]*P* $\bar{3}$ 2/*c* 1; [3]*R* $\bar{3}$ 2/*c*

II [2]*F* 1 2/*m* 1 (*C* 2/*m*); [2]*C* 1 2/*m* 1 ($2\boldsymbol{c}'=\boldsymbol{c}$)(*C* 2/*m*); [2]*P* 1 2/*c* 1 ($2\boldsymbol{a}'=\boldsymbol{a},2\boldsymbol{b}'=\boldsymbol{b}$)(*P* 2/*c*)

$C\,2/c$ C_{2h}^6 $\cdot 2/m$ Monoclinic

No. 15

UNIQUE AXIS b, DIFFERENT CELL CHOICES

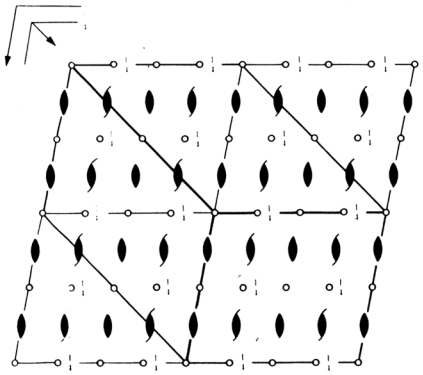

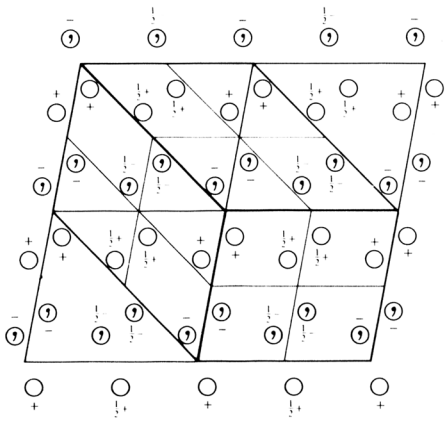

$C\,1\,2/c\,1$

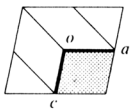

UNIQUE AXIS b, CELL CHOICE 1

Origin at $\bar{1}$ on glide plane c

Asymmetric unit $0\leq x\leq \frac{1}{2};\ 0\leq y\leq \frac{1}{2};\ 0\leq z\leq \frac{1}{2}$

Generators selected (1); $t(1,0,0)$; $t(0,1,0)$; $t(0,0,1)$; $t(\frac{1}{2},\frac{1}{2},0)$; (2); (3)

Positions

Multiplicity, Wyckoff letter, Site symmetry	Coordinates				Reflection conditions
	(0,0,0)+	$(\frac{1}{2},\frac{1}{2},0)$+			General:
8 f 1	(1) x,y,z	(2) $\bar{x},y,\bar{z}+\frac{1}{2}$	(3) $\bar{x},\bar{y},\bar{z}$	(4) $x,\bar{y},z+\frac{1}{2}$	hkl : $h+k=2n$ $0k0$: $k=2n$ $h0l$: $h,l=2n$ $h00$: $h=2n$ $0kl$: $k=2n$ $00l$: $l=2n$ $hk0$: $h+k=2n$
					Special: as above, plus
4 e 2	$0,y,\frac{1}{4}$	$0,\bar{y},\frac{3}{4}$			no extra conditions
4 d $\bar{1}$	$\frac{1}{4},\frac{1}{4},\frac{1}{2}$	$\frac{3}{4},\frac{1}{4},0$	4 c $\bar{1}$	$\frac{1}{4},\frac{1}{4},0$ $\frac{3}{4},\frac{1}{4},\frac{1}{2}$	hkl : $k+l=2n$
4 b $\bar{1}$	$0,\frac{1}{2},0$	$0,\frac{1}{2},\frac{1}{2}$	4 a $\bar{1}$	$0,0,0$ $0,0,\frac{1}{2}$	hkl : $l=2n$

CONTINUED

No. 15 $C\,2/c$

$A\,1\,2/n\,1$

UNIQUE AXIS b, CELL CHOICE 2

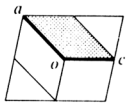

Origin at $\bar{1}$ on glide plane n

Asymmetric unit $0\leq x\leq\frac{1}{2}$; $0\leq y\leq 1$; $0\leq z\leq\frac{1}{4}$

Generators selected (1); $t(1,0,0)$; $t(0,1,0)$; $t(0,0,1)$; $t(0,\frac{1}{2},\frac{1}{2})$; (2); (3)

Positions

Multiplicity, Wyckoff letter, Site symmetry			Coordinates (0,0,0)+	Coordinates $(0,\frac{1}{2},\frac{1}{2})$+			Reflection conditions
							General:
8	f	1	(1) x,y,z	(2) $\bar{x}+\frac{1}{2},y,\bar{z}+\frac{1}{2}$	(3) $\bar{x},\bar{y},\bar{z}$	(4) $x+\frac{1}{2},\bar{y},z+\frac{1}{2}$	hkl : $k+l=2n$ $0k0$: $k=2n$ $h0l$: $h,l=2n$ $h00$: $h=2n$ $0kl$: $k+l=2n$ $00l$: $l=2n$ $hk0$: $k=2n$
							Special: as above, plus
4	e	2	$\frac{1}{4},y,\frac{1}{4}$	$\frac{1}{4},\bar{y},\frac{1}{4}$			no extra conditions
4	d	$\bar{1}$	$\frac{1}{2},\frac{1}{4},\frac{1}{2}$	$0,\frac{1}{4},\frac{1}{2}$			hkl : $h=2n$
4	b	$\bar{1}$	$0,\frac{1}{2},0$	$\frac{1}{2},\frac{1}{2},\frac{1}{2}$			hkl : $h+k=2n$
4	c	$\bar{1}$	$0,\frac{1}{4},\frac{1}{4}$	$\frac{1}{2},\frac{1}{4},\frac{1}{4}$			
4	a	$\bar{1}$	0,0,0	$\frac{1}{2},0,\frac{1}{2}$			

$I\,1\,2/a\,1$

UNIQUE AXIS b, CELL CHOICE 3

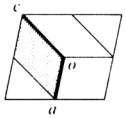

Origin at $\bar{1}$ on glide plane a

Asymmetric unit $0\leq x\leq 1$; $0\leq y\leq\frac{1}{2}$; $0\leq z\leq\frac{1}{4}$

Generators selected (1); $t(1,0,0)$; $t(0,1,0)$; $t(0,0,1)$; $t(\frac{1}{2},\frac{1}{2},\frac{1}{2})$; (2); (3)

Positions

Multiplicity, Wyckoff letter, Site symmetry			Coordinates (0,0,0)+	Coordinates $(\frac{1}{2},\frac{1}{2},\frac{1}{2})$+			Reflection conditions
							General:
8	f	1	(1) x,y,z	(2) $\bar{x}+\frac{1}{2},y,\bar{z}$	(3) $\bar{x},\bar{y},\bar{z}$	(4) $x+\frac{1}{2},\bar{y},z$	hkl : $h+k+l=2n$ $0k0$: $k=2n$ $h0l$: $h,l=2n$ $h00$: $h=2n$ $0kl$: $k+l=2n$ $00l$: $l=2n$ $hk0$: $h+k=2n$
							Special: as above, plus
4	e	2	$\frac{1}{4},y,0$	$\frac{3}{4},\bar{y},0$			no extra conditions
4	d	$\bar{1}$	$\frac{1}{4},\frac{1}{4},\frac{3}{4}$	$\frac{1}{4},\frac{1}{4},\frac{1}{4}$			hkl : $l=2n$
4	b	$\bar{1}$	$0,\frac{1}{2},0$	$\frac{1}{2},\frac{1}{2},0$			hkl : $h=2n$
4	c	$\bar{1}$	$\frac{1}{4},\frac{1}{4},\frac{3}{4}$	$\frac{3}{4},\frac{1}{4},\frac{1}{4}$			
4	a	$\bar{1}$	0,0,0	$\frac{1}{2},0,0$			

Appendix C

Crystallographic data for $SrNb_2O_6$ and $Sr_2Nb_5O_9$

We provide the crystallographic data from ICSD for the $SrNb_2O_6$ phase reported by Marinder [21] and the $Sr_2Nb_5O_9$ phase reported by Svensson [22].

C.1 The $SrNb_2O_6$ phase

```
*data for   ICSD #60782
CopyRight   ©2003 by Fachinformationszentrum Karlsruhe, and the U.S. Sec-
retary of
            Commerce on behalf of the United States.  All rights reserved.
Coll Code   60782
Rec  Date   1988/02/22
Chem Name   Strontium Diniobium Hexaoxide - Monoclinic
Structured  Sr Nb2 O6
Sum         Nb2 O6 Sr1
ANX         AB2X6
D(calc)     5.17
Title       Powder diffraction studies of SrNb2O6 and SrNb6O16
Author(s)   Marinder, B.O.;Wang, P.-L.;Werner, P.E.
Reference   Acta Chemica Scandinavica, Series A: (28,1974-)
            (1986), 40, 467-475
Unit Cell   7.7223(7) 5.5944(5) 10.9862(7) 90. 90.372(5) 90.
Vol         474.61
Z           4
Space Group P 1 21/c 1
SG Number   14
Cryst Sys   monoclinic
Pearson     mP36
Wyckoff     e9
R Value     0.1
Red Cell    P  5.594 7.722 10.986 90.372 90 90 474.612
```

```
Trans Red   0.000 -1.000 0.000 / -1.000 0.000 0.000 / 0.000 0.000 -1.000
Comments    X-ray diffraction (powder)
            At least one temperature factor missing in the paper.
Atom  #   OX   SITE      x           y           z           SOF      H
 Sr   1  +2    4 e   0.2523(7)   0.536(1)    0.0393(3)      1.         0
 Nb   1  +5    4 e   0.0143(6)   0.0294(17)  0.1448(4)      1.         0
 Nb   2  +5    4 e   0.5232(6)   0.4698(16)  0.6428(4)      1.         0
 O    1  -2    4 e   0.044(4)    0.228(6)    0.975(3)       1.         0
 O    2  -2    4 e   0.456(4)    0.262(7)    0.467(3)       1.         0
 O    3  -2    4 e   0.070(4)    0.376(5)    0.206(3)       1.         0
 O    4  -2    4 e   0.454(4)    0.129(5)    0.701(3)       1.         0
 O    5  -2    4 e   0.258(4)    0.963(5)    0.149(2)       1.         0
 O    6  -2    4 e   0.758(5)    0.149(4)    0.116(2)       1.         0
*end for    ICSD #60782
```

C.2 The $Sr_2Nb_5O_9$ phase

```
*data for   ICSD #68884
CopyRight   ©2003 by Fachinformationszentrum Karlsruhe, and the U.S. Sec-
retary of
            Commerce on behalf of the United States.  All rights reserved.
Coll Code   68884
Rec  Date   1992/01/20
Chem Name   Strontium Niobium(II) Niobium Oxide (2/1/4/9)
Structured  Sr2 Nb Nb4 O9
Sum         Nb5 O9 Sr2
ANX         A2BC4X9
D(calc)     6.3
Title       High resolution electron microscopy and X-ray powder diffraction
            studies of Sr2Nb5O9
Author(s)   Svensson, G.
Reference   Acta Chemica Scandinavica (43,1989-)
            (1990), 44, 222-227
Unit Cell   4.1405(4) 4.1405(4) 12.040(2) 90. 90. 90.
Vol         206.41
Z           1
Space Group P 4/m m m
SG Number   123
Cryst Sys   tetragonal
Pearson     tP16
Wyckoff     i h2 g f e c b
R Value     0.18
Red Cell    P  4.140 4.140 12.04 90 90 90 206.411
Trans Red   1.000 0.000 0.000 / 0.000 1.000 0.000 / 0.000 0.000 1.000
Comments    X-ray diffraction (powder)
            At least one temperature factor missing in the paper.
Atom  #   OX   SITE      x           y           z           SOF      H
 Sr   1  +2    2 g   0           0           0.1694         1.         0
 Nb   1  +2.5  2 e   0           0.5         0.5            1.         0
 Nb   2  +2.5  2 h   0.5         0.5         0.328          1.         0
 Nb   3  +4    1 c   0.5         0.5         0              1.         0
```

```
 O    1  -2    2 f   0.5         0           0              1.          0
 O    2  -2    2 h   0.5         0.5         0.165          1.          0
 O    3  -2    4 i   0.5         0           0.329          1.          0
 O    4  -2    1 b   0           0           0.5            1.          0
*end for    ICSD #68884
```

Bibliography

[1] International energy outlook 2002. Technical Report DOE/EIA-0484(2002), Energy Information Administration/US Department of Energy, Washington DC, March 2002.

[2] M. S. Dresselhaus and I. L. Thomas. Alternative energy technologies. *Nature*, 414:332–337, 2001.

[3] Brian C. H. Steele and Angelika Heinzel. Materials for fuel-cell technologies. *Nature*, 414:345–352, 2001.

[4] Truls Norby. Fast oxygen ion conductors—from doped to ordered systems. *Journal of Materials Chemistry*, 11:11–18, 2001.

[5] M. Tanaka, R. Saito, and D. Watanabe. Symmetry determination of the room-temperature form of $LnNbO_4(Ln = La, Nd)$ by convergent-beam electron diffraction. *Acta Crystallographica*, A36:350–352, 1980.

[6] S. Tsunekawa and H. Takei. Twinning structure of ferroelastic $LaNbO_4$ and $NdNbO_4$ crystals. *Physica status solidi*, A 50:695–702, 1978.

[7] Li Jian and C. Marvin Wayman. Domain boundary and domain switching in a ceramic rare-earth orthoniobate $LaNbO_4$. *Journal of the American Ceramic Society*, 79(6):1642–1648, 1996.

[8] Kêitsiro Aizu. Possible species of ferromagnetic, ferroelectric, and ferroelastic crystals. *Physical Review B*, 2(3):754–772, 1970.

[9] Kêitsiro Aizu. Determination of the state parameters and formulation of spontaneous strain for ferroelastics. *Journal of the Physical Society of Japan*, 28(3):706–716, March 1970.

[10] A. G. Khachaturyan. *Theory of structural transformations in solids*. John Wiley & Sons, New York, 1983.

[11] J. Sapriel. Domain-wall orientations in ferroelastics. *Physical Review B*, 12(11):5128–5140, 1975.

[12] John L. Schlenker, G. V. Gibbs, and Monte B. Boisen Jr. Strain-tensor components expressed in terms of lattice parameters. *Acta Crystallographica*, A34:52–54, 1978.

[13] W. I. F. David. The high-temperature paraelastic structure of $LaNbO_4$. *Materials Research Bulletin*, 18:749–756, 1983.

[14] Li Jian and C.M. Wayman. Monoclinic-to-tetragonal phase transformation in a ceramic rare-earth orthoniobate, $LaNbO_4$. *Journal of the American Ceramic Society*, 80(3):803–806, 1997.

[15] S. Tsunekawa, T. Kamiyama, K. Sasaki, H. Asano, and T. Fukuda. Precise structure analysis by neutron diffraction for $RNbO_4$ and distortion of NbO_4 tetrahedra. *Acta Crystallographica*, A49:595–600, 1993.

[16] I. D. Brown. Chemical and steric constraints in inorganic solids. *Acta Crystallographica*, B48:553–572, 1992.

[17] I. D. Brown and D. Altermatt. Bond-valence parameters obtained from a systematic analysis of the inorganic crystal structure database. *Acta Crystallographica*, B41:244–247, 1985.

[18] Line Klavenes Berg. A transmission electron microscope study of the transition from amorphous to crystalline state of some metallic glasses. Master's thesis, University of Oslo, Department of Physics, June 1996.

[19] Arne Olsen. The theory and practice of analytical electron microscopy in materials science. Department of Physics, Univeristy of Oslo, 2002.

[20] D. de Fontaine and L. T. Wille ans S.C Moss. Stability analysis of special-point ordering in the basal-plane in $YBa_2Cu_3O_{7-\delta}$. *Physical Review B*, 36(10):5709–5712, 1987.

[21] Bengt-Olov Marinder, Pei-Ling Wang, and Per Erik Werner. Powder diffraction studies of $SrNb_2O_6$ and $SrNb_6O_{16}$. *Acta Chemica Scandinavica A*, 40:467–475, 1986.

[22] Gunnar Svensson. High resolution electron microscopy and X-ray powder diffraction studies of $Sr_2Nb_5O_9$. *Acta Chemica Scandinavica*, 44:222–227, 1990.

[23] Theo Hahn, editor. *International tables for crystallography*, volume A Space-Group Symmetry. D. Reidel Publishing Company, Boston, 1983.